Journal of
Materials Chemistry C

ROYAL SOCIETY OF CHEMISTRY

REVIEW

View Article Online
View Journal | View Issue

Cite this: J. Mater. Chem. C, 2023, 11, 2430

Recent advances in single crystal narrow band-gap semiconductor nanomembranes and their flexible optoelectronic device applications: Ge, GeSn, InGaAs, and 2D materials

Shu An,† HyunJung Park and Munho Kim *

Received 27th November 2022,
Accepted 16th January 2023

DOI: 10.1039/d2tc05041b

rsc.li/materials-c

Flexible optoelectronics have attracted much attention in recent years for their potential applications in healthcare and wearable devices. Narrow bandgap (NBG) semiconductor nanomembranes (NMs) are promising candidates for flexible near-infrared (NIR) applications due to their light weight, bendability, and excellent material properties (*e.g.*, fast carrier mobility and appropriate bandgap energy). However, a comprehensive summary of the current research on the NBG NMs has not been provided yet. This review highlights recent advances in the development of NBG semiconductor NMs, including Group IV (*e.g.*, Ge and GeSn) and III–V (*e.g.*, InGaAs) compounds, and 2D materials (*e.g.*, black phosphorus and graphene) and their applications in flexible optoelectronics. The material growth, fabrication process, and characterization of material properties are summarized. Moreover, abundant applications in flexible devices are present, including but not limited to photodetectors, light emitting diodes, and lasers.

1. Introduction

Semiconductors with band-gap energy less than 2.3 eV are defined as narrow band-gap semiconductors (NBGs).[1] Typically, representative examples of such semiconductors are Group IV

School of Electrical and Electronic Engineering, Nanyang Technological University, 50 Nanyang Avenue, 639798, Singapore, Singapore. E-mail: munho.kim@ntu.edu.sg
† These authors contributed equally

Shu An

*Shu An received her BS and MS degrees in Precision Instrument and Technology from Wuhan University and Tsinghua University, China, respectively. She received her PhD degree in the School of Electrical and Electronic Engineering at the Nanyang Technological University under the supervision of Prof. Munho Kim. After getting her PhD in 2022, she moved to Agency for Science, Technology and Research (A*STAR), Singapore to become a scientist working on nanofabrication and metasurface.*

HyunJung Park

HyunJung Park is a research fellow in the School of Electrical and Electronic Engineering at the Nanyang Technological University, Singapore. She received her BS and PhD in the Department of Materials Science and Engineering from Korea University, Seoul, Korea, under Prof. Donghwan Kim, in 2015 and 2020, respectively. She became a research professor in Brain Korea 21 of the Department of Materials Science and Engineering at Korea University, Seoul, Korea, in 2020 and a visiting researcher in PV-Lab at EPFL, Neuchâtel, Switzerland, for 2021. In 2022, she joined Prof. Munho Kim's Nano Engineering Device Laboratory at Nanyang Technological University, Singapore, as a research fellow. Currently, her research interests focus on the fabrication of optoelectronic devices using various types of semiconductors and the application of nanotechnologies on photonic devices.

Open Access Article. Published on 20 January 2023. Downloaded on 9/14/2024 7:34:49 AM.
This article is licensed under a Creative Commons Attribution-NonCommercial 3.0 Unported Licence.

This journal is © The Royal Society of Chemistry 2023

Open Access Article. Published on 20 January 2023. Downloaded on 9/14/2024 7:34:49 AM.
This article is licensed under a Creative Commons Attribution-NonCommercial 3.0 Unported Licence.

(*e.g.*, Si, Ge, and GeSn) and III–V (*e.g.*, InAs and InGaAs) compounds, and two-dimensional (2D) materials (*e.g.*, black phosphorus (BP) and graphene), which are shown in Table 1. These NBG materials have two outstanding advantages in respect of optoelectronic and electronic applications due to their small band-gap energies. First, NBGs are suitable for applications in near infrared (NIR) devices ranging from imaging and sensing to communication.[2–5] Second, the carrier mobility is higher than that of wide band-gap materials, facilitating the development of high-speed devices and circuits. Numerous research studies have been devoted to NBG materials and their device applications. However, application to flexible devices has been limited, which emphasizes the need for developing new materials and integration technologies. During the development of nanotechnology in the past decades, nanowires (NWs) and nanomembranes (NMs) have been regarded as the most important structures of materials, attracting enormous research interest. NWs and NMs both showed great promise in a wide range of applications for flexible electronic devices, especially in the wearable and healthcare areas.[6,7]

Semiconductor NWs, a one-dimensional nanostructure with a diameter of a few nanometers and a length in the micrometer scale, are the fundamental building block of both electronic[8] and photonic devices.[9–11] However, the quality of NWs depends crucially on substrates and growth methods.[12] Compared with NWs, NM materials are more compatible with device fabrication and packaging as they cover a larger scale area.[13] In addition, NMs are extremely attractive for high-performance flexible photonic applications because of their excellent material properties (*e.g.*, fast carrier mobility and high absorption capability) and strong bendability. Their ultrathin thickness not only guarantees high mechanical flexibility and extreme material uniformity but also ensures their durability and performance stability after bending multiple times. Furthermore, the fabrication methods of free-standing NBG NMs are well established. It is feasible to achieve high-quality NMs with superior uniformity and scalability through a careful control of the process, laying the foundation for industrial production.[14] Another unneglectable advantage of free-standing NBG NMs is the suitable material platform for strain application. Strain plays a key role in modulating the optical and electrical properties of semiconductors. In other words, strain significantly modifies the band structure and has the potential to improve carrier mobility and hence device performance.[15–25]

Fig. 1 summarizes the application chart that indicates the potential or current use of optical (*e.g.* photodetectors (PDs), light emitting diodes (LEDs) and lasers) and electrical devices (*e.g.* power electronics and radio frequency) based on various free-standing NBG membranes covered in this review. Ge NM has been explored widely as an active layer for enhanced absorption and emission properties in devices.[15,20,26–31] A. Gassenq *et al.* suggested that biaxially strained Ge can be a suitable platform for realizing high-performance lasers.[32,33] GeSn has considerable potential for NIR PD applications due to its direct band-gap and excellent compatibility with the complementary metal-oxide semiconductor (CMOS) process. In addition, GeSn shows significant benefits in forming high-performance lasers with low threshold and high operation temperature. However, Ge/GeSn based optoelectronic devices show a high dark current, which hinders their commercialization. InGaAs is one of the most popular materials used to fabricate commercial NIR PDs. Although the detection range is limited to 1700 nm, it covers most optical communication bands (O-band to L-band) of conventional Si fibers.

2D materials are atomically thin crystalline solids, existing in the form of one or few-layered sheets where each layer is bound by van der Waals (vdW) force. So far, 2D materials have aroused tremendous research interest due to their outstanding and unique material properties such as large surface area, nanoscale thickness, flexibility, and remarkable optoelectronic properties. These material properties allow 2D materials to be considered as one of the most promising candidates for the applications of optoelectronic devices. Graphene, the firstly discovered 2D material, has been extensively studied and applied to versatile optical and electronic devices because of its exceptional thermal and electrical conductivity with flexibility.[34–36] Black phosphorous (BP) is an emerging 2D material that has distinctive material properties, which include not only high conductivity and carrier mobility but also tunable direct band-gap, unlike graphene. This tunable band-gap of BP enables a wide range of devices applications.[37,38]

Free-standing NBG NMs are promising material platforms for various applications. However, there is no comprehensive review focused on NBG NMs so far. Therefore, in this paper, we provide a comprehensive review on the recent progress of NBG NMs. Representative NBG NMs are discussed, including

Munho Kim

Munho Kim received his BS and MS degrees in Electrical Engineering from Pohang University of Science & Technology, Pohang, and Korea Advanced Institute of Science & Technology, Daejeon, South Korea, in 2007 and 2009, respectively. From 2009 - 2010, he was a member of the R&D team at Samsung Semiconductor Research Center, Hwaseong, South Korea. He received his PhD degree in the Department of Electrical and Computer Engineering from the University of Wisconsin-Madison in 2016. In 2016, he became a postdoctoral research associate in the Department of Electrical and Computer Engineering at the University of Illinois at Urbana-Champaign. He is currently an assistant professor in School of Electrical and Electronic Engineering at the Nanyang Technological University, Singapore. His research interests mainly focus on the development of nanostructured semiconductor materials and devices for unconventional electronic and photonic applications.

Table 1 List of NBG semiconductors and their important material properties covered in this review

	Si	Ge	GeSn	GaAs	InGaAs	BP	Graphene
Band-gap (eV)	1.12	0.66	0.4–0.66	1.43	0.36–1.425	0.3–2.0[39]	0[40]
Dielectric constant	11.9	16.2	0.4–4.5	13.1	13.9[41]	2.9–8.3[42]	1.8–3[43]
Electric breakdown field (kV cm^{-1})	300	100	100[44]	400	200	N/A	N/A
Electron mobility (cm^2 V^{-1} s^{-1})	1400	3900	698[45]	8500	1200	1000[46]	4500[47]
Hole mobility (cm^2 V^{-1} s^{-1})	450	1900	540[48]	400	300	1000[49]	4500[47]
Thermal conductivity (W cm^{-1} K^{-1})	1.5	0.58	0.04	0.46	0.014[50]	4000[51]	5000[52]
Saturated electron drift velocity ($\times 10^7$ cm s^{-1})	1	0.65	N/A	1	2.95	1[53]	3[47]

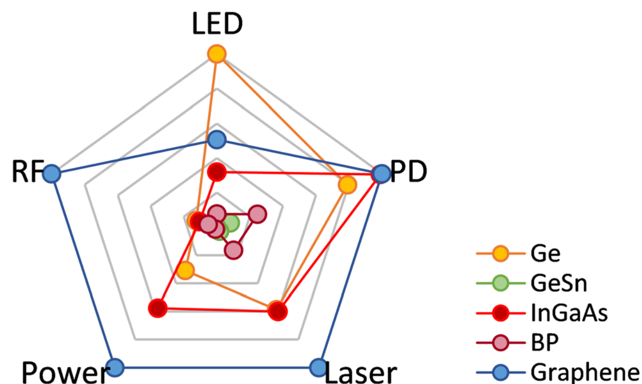

Fig. 1 Application chart of single crystalline free-standing NBG NMs in the photodetector (PD), laser, light emitting diodes (LED), radio frequency (RF) and power electronics based on the number of publications. Data are collected by keyword search from Web of Science (year of search: 2022).

Ge, GeSn, InGaAs, and 2D materials (BP and graphene). Our review covers material characteristics, fabrication methods, and device applications. Finally, we present the conclusion and major challenges and future perspectives on single crystalline NBG materials.

2. Ge and GeSn nanomembranes

NMs are monocrystalline structures with a thickness of a few hundred nanometers, leading to the advantages of flexibility, bendability, and light weight. The main difference from thin films is that NMs can exist as a free-standing form, either at certain critical stages of their growth or processing or at steps with the final device-integrated form.

Ge has been widely explored as a platform for optoelectronic devices due to its CMOS capability. Although it is an indirect band-gap semiconductor, the energy difference between the lowest indirect L and direct Γ valleys is only 136 meV as indicated in Fig. 2(a). Additionally, the introduction of tensile strain or incorporation of Sn can effectively compensate for the small difference, which turns Ge into a direct band-gap semiconductor.[54,55] Numerous studies have shown that the band-gap structure of Ge can be modulated from indirect to direct by applying tensile strain. On the other hand, the incorporation of Sn into Ge also changes the electronic band structure by shrinking L and Γ valleys simultaneously while Γ valleys drop faster than L valleys (Fig. 2(b)). As shown in Fig. 2(c), there is a crossover point of band-gap transition when Sn composition increases to 8%, indicating that 8% of Sn successfully changes Ge to a direct band-gap semiconductor under no external strain conditions. However, the Sn content is limited by the compressive strain resulted from lattice mismatch between Sn and Ge.

2.1. Strategies to fabricate GeSn NMs

Typically, the formation of GeSn NMs begins with GeSn on an insulator (GeSnOI) or GeSn on an Si-on-insulator (SOI) platform. As illustrated in Fig. 3, wet and dry etching are the most common methods to fabricate GeSn NMs. To give an example of GeSnOI, (Fig. 3(a)) array patterns of etching holes (size of 3×3 μm^2 and distance of 50 μm) are created on the cleaned substrates followed by reactive ion etching (RIE) to etch down

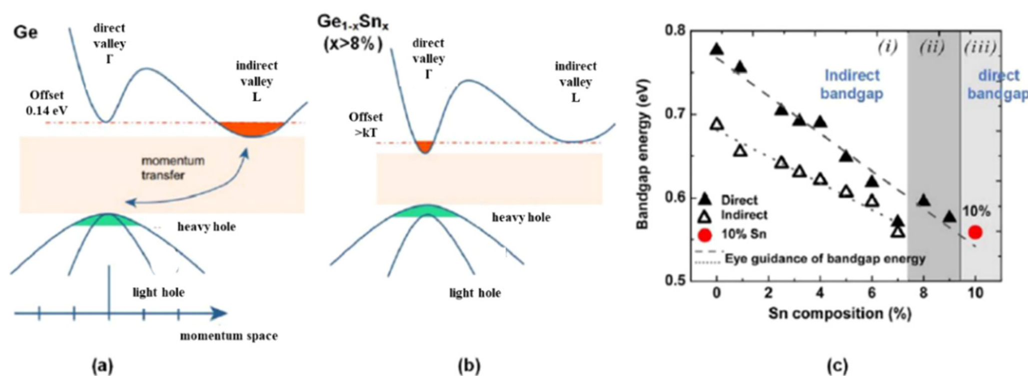

Fig. 2 Energy band structure of (a) undoped Ge bulk with indirect bandgap and (b) GeSn alloying with Sn composition higher than 8% with direct bandgap without mechanically introducing strain. (c) The indirect-to-direct transition of GeSn band-gap energy as a function of Sn composition.[56]

Open Access Article. Published on 20 January 2023. Downloaded on 9/14/2024 7:34:49 AM.
This article is licensed under a Creative Commons Attribution-NonCommercial 3.0 Unported Licence.

This journal is © The Royal Society of Chemistry 2023

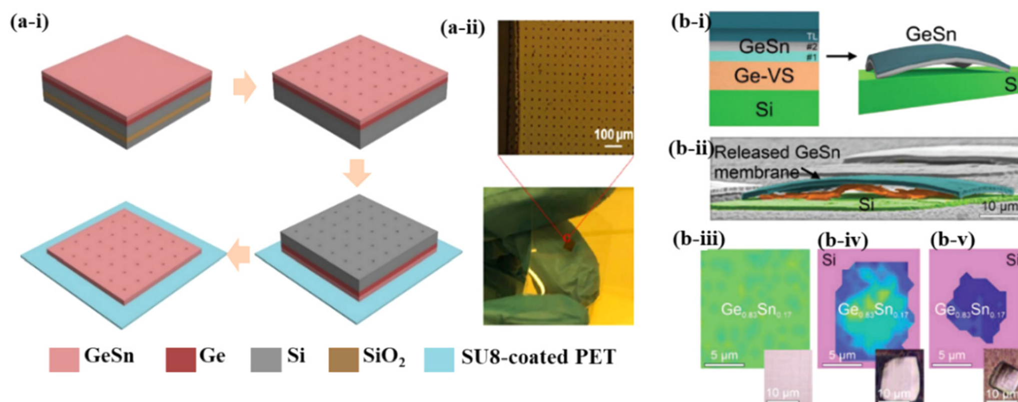

Fig. 3 Schematic illustration of the most common methods used to fabricate GeSn NMs. (a) Wet etching:[13] (i) Preparation of strain-free GeSn NMs by patterning an array of etching holes followed by RIE, HF undercut, and transfer printing. (ii) Optical images of GeSn NMs on PET with its magnified microscopic image. Reproduced with permission from ref. 13. Copyright 2020, IOP Publishing. (b) Dry etching:[57] (i) Fabrication of GeSn NMs by anisotropic etching of GeSn sidewalls using Cl_2-based plasma, followed by CF_4-based selective etching of buffer Ge layer. (ii) SEM of a solitary released GeSn membrane and (iii–v) Raman spectroscopy maps for an as-grown GeSn layer, partially suspended and fully released GeSn membrane, respectively. Reproduced with permission from ref. 57. Copyright 2020, Wiley-VCH.

Open Access Article. Published on 20 January 2023. Downloaded on 9/14/2024 7:34:49 AM. This article is licensed under a Creative Commons Attribution-NonCommercial 3.0 Unported Licence.

to the sacrificial layer. These etching holes act as a pathway for etching solutions to reach the oxide layer, which leads to rapid and uniform undercut. Subsequently, SiO_2 sacrificial layer is removed by dipping in hydrofluoric acid (HF, 49%), releasing top GeSn/Ge template layers. The released NMs are then transfer printed to a SU-8 coated polyethylene terephthalate (PET) substrate using a direct flip transfer method. Another transfer printing process using a polydimethylsiloxane (PDMS) stamp can also replace this step as long as NM is present as the uppermost layer. Finally, the layers on top of GeSn (*e.g.*, buffer Ge and Si) are etched by an SF_6-based RIE to create fully relaxed flexible GeSn NMs.

Fig. 3(b) shows another approach to obtain GeSn NMs namely a dry release approach. The starting material is GeSn on Ge virtual layer grown on an Si substrate. It begins with the anisotropic Cl_2-based RIE of the GeSn sidewalls, followed by a CF_4-based selective etching of the Ge layer. Although the process is relatively simple, the size of NMs (20×20 μm^2) is limited by etching the selectivity between GeSn and the buffer Ge layer.

Etching holes facilitate the wet etching process and therefore no obvious residuals exist due to the adequate chemical reaction and good selectivity. However, CF_4-based dry etching with low selectivity results in a damaged GeSn surface due to over-etching. By changing the power and pressure of RIE, the residual can be reduced by the enhanced selectivity. Although wet and dry etchings are promising to release Ge/GeSn membranes form source wafers, it is still a great challenge to fabricate large-size strain-free GeSn membranes with high Sn content and good surface quality. Moreover, the fabrication of ultrathin GeSn membranes with a thickness of less than 100 nm is also challenging. A higher undercut temperature and a more diluted etchant provide a feasible way to produce large-sized uniform membranes by promoting the contact between the etchant and the sacrificial layer.

2.2. Strain engineering

Strain engineering is an essential research topic for GeSn NMs because their ultra-thin thickness (nm) enables the application of the strain by various methods. Practically, the methods used to apply strain can be divided into two categories depending on the type of applied strain: (i) internal strain generated during the growth process; (ii) external strain applied on well-prepared flexible GeSn NMs using mechanical testing equipment or home-made mechanical tools.

Among versatile approaches for applying internal strain, one of the most popular methods is to utilize high-stress layers, which act as an extrinsic stressing agent to introduce biaxial tensile strain.[58] C. S. Fenrich *et al.* deposited 260 nm SiN_y on $Ge_{0.934}Sn_{0.066}$ multiple quantum well microdisk, creating a direct band-gap by elimination of local biaxial strain. Another form of internal strain engineering is the rolling up, which is used to fabricate micro-resonators. Fig. 4(b) illustrates the rolling up method where GeSn NMs were rolled up from the sample with pre-defined U-shape patterns formed by lithography and RIE and subsequent HF etching. The undercutting process releases NMs from the substrates by self-rolling from the lower side of the U-shape, which is resulted from different strain in each layer. The fabricated micro-resonator with this structure showed a high quality factor (Q factor) of up to 800.[59]

In addition to the techniques mentioned above, new technologies for applying strain on flexible Ge or GeSn NMs have been developed, as shown in Fig. 4(c) and (d). Fig. 4(c) shows the flexible Ge NM on polyethylene terephthalate (PET) film obtained by wet etching or dry etching, and herein, strains were introduced by externally applied gas pressure.[60,61] Furthermore, uniform biaxial strain can be introduced through the expanding surface sphere, as the increase of the injected gas into the cavity causes the transformation of the top plane into a hemispherical shape. This technique could introduce various accurate minor strains, but the setup is complicated. Another approach to induce strain is to utilize bending fixtures with various radii. In this method, the bending fixture induces specific strain values by placing flexible NMs directly on the concave or convex fixture. The advantage of this approach is

Open Access Article. Published on 20 January 2023. Downloaded on 9/14/2024 7:34:49 AM.
This article is licensed under a Creative Commons Attribution-NonCommercial 3.0 Unported Licence.

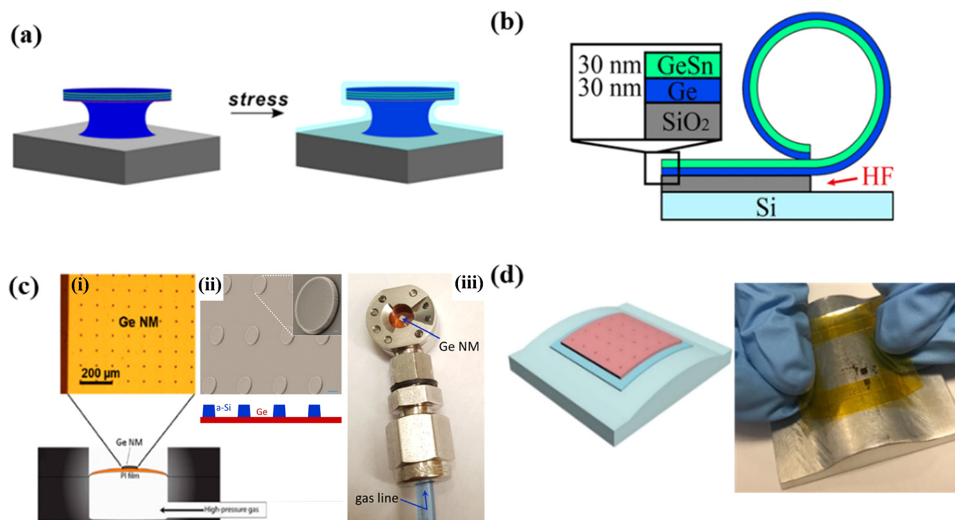

Fig. 4 Various strain-engineering strategies for GeSn NMs: (a) Tensile strained GeSn microdisk using high-stress SiN_y stressor layer.[58] Reprinted with permission from ref. 58. Copyright 2016, American Chemical Society. (b) A schematic diagram describing the rolling up procedure for the GeSn/Ge bilayer.[59] Reproduced with permission from ref. 59. Copyright 2018, IOP Publishing. (c) (i) Schematic illustration of the experimental setup for biaxial tensile strained Ge NMs,[60] (ii) SEM image with a schematic of a Ge NM coated with an a-Si pillar array, and a photograph of the pressure cell loaded with a Ge NM.[61] Reproduced with permission from ref. 60 and 61. Copyright 2018, 2021, MDPI, American Chemical Society. (d) Schematic structure and optical image of flexible GeSn NMs where uniaxial strains are introduced by placing conformally on bending fixtures.[62] Reproduced with permission from ref. 62. Copyright 2021, IOP Publishing.

that the method is simpler than the gas pressure method. In addition, we can introduce uniaxial compressive strain to investigate its effect on the optoelectronic properties. However, one disadvantage is that only a specific strain can be introduced with one bending fixture, *i.e.* each bending condition requires one fixture. Using this bending fixture-based method, the applied strain can be evaluated using various analysis techniques. One example is Raman spectroscopy which has the advantageous feature that the system is highly sensitive with easy operation. Previously, several researchers have studied the relationship between the Raman shift and biaxial or uniaxial strain induced in flexible GeSn with different Sn compositions.[62] Overall, internal or external strain can be easily introduced into GeSn by using stress layers or mechanical tools. However, the applicable area with a uniform strain is limited.

2.3. Applications of strain engineered GeSn nanomembranes

2.3.1. Optical sensors. GeSn NMs have attracted much attention for applications in optoelectronic devices, such as PDs,[15,64] lasers, resonators,[59] and waveguides due to their outstanding electronic and optical properties. The principle of PDs exploiting the photon effects is to convert the absorbed incident photons into electrical signals. Electrons in the valence band absorb the photons with energy greater than the bandgap of the functional semiconductors and jump into the empty conduction band, leaving a hole in the valence band, thereby creating abundant electron–hole pairs (EHPs). The incident photons are converted to photocurrent or voltage, completing the transformation of the light signal to the electric signal. The important figure-of-merits to evaluate the performance of PDs include dark current (I_{dark}), responsivity (R), detectivity (D^*), rise time, and bandwidth. Dark current is defined as the current measured under dark conditions. It is a critical parameter to evaluate PD performance, being considered as noise. Responsivity, one of the representative parameters to evaluate the optical response, is determined by the net photocurrent generated upon excitation of unit incident power. Specific detectivity is a commonly used parameter to evaluate the capability of devices to detect weak optical signals, which is defined as the inverse of the noise-equivalent power (NEP). Rise time, also known as response time, is derived by calculating the time required for the PDs to increase photocurrent from 10% to 90% of the maximum photocurrent. Rise time also can be used to estimate how fast the PDs respond to a step light input signal. The response bandwidth is generally represented by the −3dB bandwidth, which refers to the corresponding frequency bandwidth when the responsivity is reduced to half of the maximum value.

Although the thinness of GeSn NMs reduces absorption, the external strain and high Sn composition could offset the reduced absorption by modulating the band-gap structure, which enhances the absorption coefficient. Fig. 5(a) illustrates the fabricated flexible GeSn PDs and their performance characterization. Flexible Ge/GeSn NMs with 8% Sn content were released by wet etching, followed by mesa patterning and RIE to make rectangular mesa (90 × 100 μm^2). Finally, interdigitated pads were deposited to form metal contacts (Fig. 5(a-i) and (a-ii)). As shown in Fig. 5(a-iii), dark current was increased by tensile strain, while it was slightly decreased by compressive strain. This trend was similar to photocurrent, showing that it was in accordance with strain-dependent modulation of the band-gap and corresponding change in absorption coefficient. In addition, responsivity at a wavelength of 2000 nm was enhanced to 3.68 mA W^{-1} by tensile strain, proving that high performance flexible NIR GeSn PD has been achieved.

 This journal is © The Royal Society of Chemistry 2023

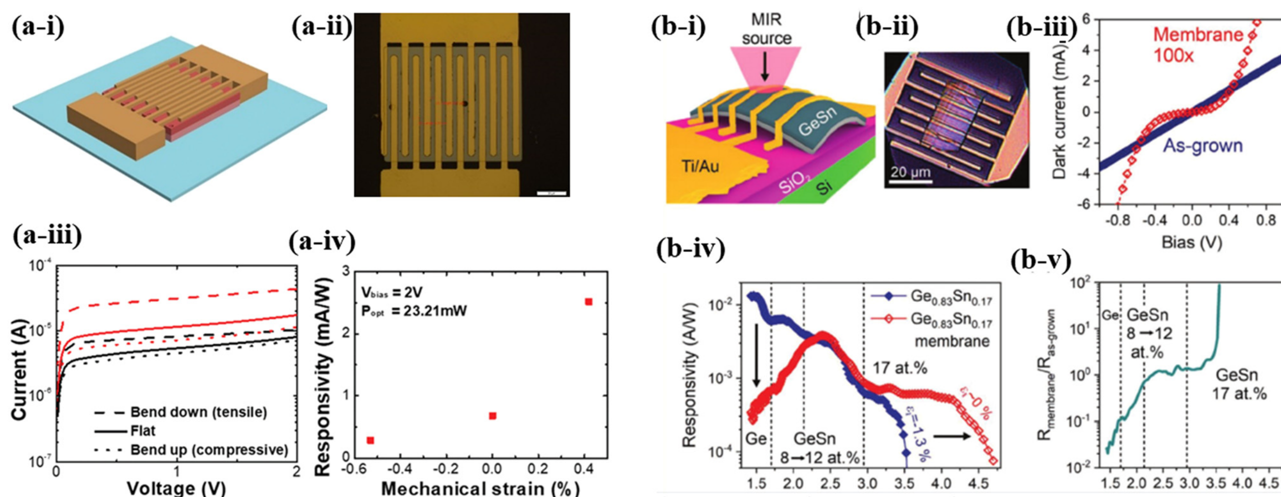

Fig. 5 (a) Device structure and characteristics of flexible GeSn metal semiconductor metal (MSM) NM PD:[19] (i) & (ii) Schematic and an optical image of the device structure, (iii) dark current and photocurrent under flat and bending conditions, and (iv) responsivity at 2000 nm as a function of mechanical strains. Reproduced with permission from ref. 19. Copyright 2020, Royal Society of Chemistry. (b) Structure and characteristics of GeSn NM PD on SiO_2/Si: (i) & (ii) Schematic and an optical image of a fabricated device, (iii) dark current *versus* bias voltage, (iv) responsivity *versus* wavelength of as-grown and membrane devices, and (v) spectral responsivity ratio of the membrane and the as-grown GeSn device.[63] Reproduced with permission from ref. 63. Copyright Copyright 2020, Wiley-VCH.

The responsivities can be further improved to 148.5 mA W^{-1} at 1550 nm by integration of TiN.[65] To expand its application into mid-IR (MIR) optoelectronic devices, a PD with an extended cut-off wavelength of 4.6 μm has been reported using fully released $Ge_{0.83}Sn_{0.17}$ NMs.[57] A dry etching based release process drastically reduces the internal compressive strain caused by lattice mismatch. Then, the released GeSn NMs were transferred onto bulk SiO_2/Si, and next, the device was fabricated by depositing interdigitated pad (Fig. 5(b-i) and (b-ii)). Although it is not intended for flexible device applications, it showed outstanding performance from the aspect of responsivity and cut-off wavelength. Fig. 5(b-iii) shows that the dark current of GeSn membrane PD was decreased by two orders compared to that of the as-grown GeSn PD because the highly conductive Ge-virtual substrate (VS)/Si stacking was replaced by an insulating substrate underneath. The responsivity of two PDs is similar in the wavelength range from 2.3 to 3.2 μm. At the longer wavelength region, the as-grown GeSn PD reached a sudden cut-off at 3.5 μm, while the membrane-based device exhibited constant responsivity up to 4.2 μm until reaching a cut-off wavelength of 4.6 μm due to strain relaxation. This study demonstrates that strain-relaxed GeSn NM is a great candidate for broad MIR range PDs. However, the flexible PDs exhibit high dark current, low quantum efficiency and slow response time compared with the rigid counterpart. The dark current can be suppressed by surface passivation processes combined with post-growth annealing to reduce the effect of defect trapping of charge carriers. Additionally, the device structure could also be optimized to reduce the carrier transit time to enhance responsivity and response speed. Light trapping through nanostructure including resonant cavity, photonic bandgap engineering, and plasmonic absorption enhancement can also be explored in this system to enhance the external quantum efficiency of the flexible GeSn PDs.

2.3.2. Light emitting application. A laser is one of optoelectronic devices that emits the coherent light at a specific wavelength, considered as an indispensable component of photonic integrated circuits. Lasing wavelength, operating temperature, and threshold current are key parameters for lasers. The lasing wavelength is determined by the bandgap of the semiconductor, and the operating temperature is the temperature that enables the lasing. The threshold current clearly separates the spontaneous and stimulated emission regime.

GeSn NM is a promising candidate material for lasers due to the direct band-gap structure. There has been substantial progress in laser technologies for achieving high-performance GeSn NM lasers with low threshold and high operating temperature. The first demonstration of Ge/GeSn/Ge quantum-well microdisk resonator with high Q factor was reported in 2014, laying the foundation for GeSn-based lasers.[59,66] A GeSn laser with direct band-gap was achieved by undercut GeSn on Ge microdisk structures with additional strain introduced by silicon nitride stressor layers, leading to enhanced photoluminescence (PL) intensity and extended PL emission range to 3–5 μm.[67] However, the PL intensity decreases dramatically by increasing temperature, which severely limits the device operating temperature as well as its real-life applications. V. Reboud *et al.* attributed the improvement of the lasing temperature up to 180 K using GeSn layers with a higher Sn composition of 16% and optimized crystalline quality.[68] The operating temperature was further increased to 230 K by employing a thicker GeSn optically active layer and a stronger carrier confinement effect in a double heterostructure.[69] A laser using GeSn photonic crystal membrane was demonstrated by Q. M. Thai *et al.* with fine performance. This approach has the potential for flexible device applications as the device was fabricated on the released layers rather than non-deformable microdisk.[70] Flexible laser

Open Access Article. Published on 20 January 2023. Downloaded on 9/14/2024 7:34:49 AM. This article is licensed under a Creative Commons Attribution-NonCommercial 3.0 Unported Licence.

Open Access Article. Published on 20 January 2023. Downloaded on 9/14/2024 7:34:49 AM.
This article is licensed under a Creative Commons Attribution-NonCommercial 3.0 Unported Licence.

Table 2 Summary of key parameters for GeSn NMs based lasers

Sn content	GeSn layer	Strain	Method	Wavelength	Threshold	Temperature
10.7%[67]	40 nm	Tensile	SiN_x stressor layer	3000 nm	low	20 K
16%[68]	400 nm	Zero	Micro-disk	3100 nm	377 kW cm^{-2}	180 K
16%[69]	850 nm	Compressive	Micro-disk	3200 nm	790 kW cm^{-2}	230 K
16%[70]	520 nm	Compressive	Step graded GeSn buffer	2880 nm	227 kW cm^{-2}	15 K
5.4%[72]	300 nm	Tensile	SiN_x stressor layer	2500 nm	0.8 KW cm^{-2}	100 K
7%[73]	500 nm	Compressive	Micro-disk	2300 nm	10 kW cm^{-2}	25 K

made on Ge NM integrated with photonic-crystal cavities with Si-pillar arrays have shown PL intensity increase due to strong optical coupling between Ge NM and the cavities. This device still preserves the mechanical flexibility advantage of NMs.[71] Recently, some breakthroughs have been made in the field of low threshold laser. A. Elbaz *et al.* reported an ultra-low threshold laser with 0.8 kW cm^{-2} based on the GeSn substrate with low Sn content.[72] A higher Sn composition makes it easier to realize direct band-gap lasers, but it also generates defects that degrade the laser performance. Therefore, finding an appropriate balance between defect engineering and Sn composition is the key to reducing the threshold of GeSn laser.[73] The key parameters of GeSn NMs based lasers are summarized in Table 2.

For MIR optoelectronic devices, many researchers have attempted to utilize other Group IV materials, such as Ge waveguide integrated MIR devices. In 2016, Wei *et al.* demonstrated Ge-on-SiN waveguides with large core-clad index contrast by wafer bonding and layer transfer technique. They employed chemical mechanical polishing (CMP) to remove the misfit dislocation between Ge and Si after the layer transfer process. The results showed that the fabricated waveguide had a propagation loss as low as 3.35 dB cm^{-1} at the wavelength of 3.8 μm.[74] Advanced material platform was proposed recently by W. Li *et al.*, with an optimized structure using GaF_2 and Y_2O_3 as cladding where the waveguiding performance was enhanced by a larger difference of refractive indexes between Ge and insulator. As a result, the proposed Ge waveguide platform showed improved performance by covering the MIR wavelength range up to 13 μm.[75]

3. InGaAs NMs

3.1. Fabrication process

InGaAs, a III–V semiconductor with a band-gap of 0.75 eV, is the most common material used for commercial NIR photodiode, taking advantage of room temperature operation with high electron mobility, external quantum efficiency, sensitivity,

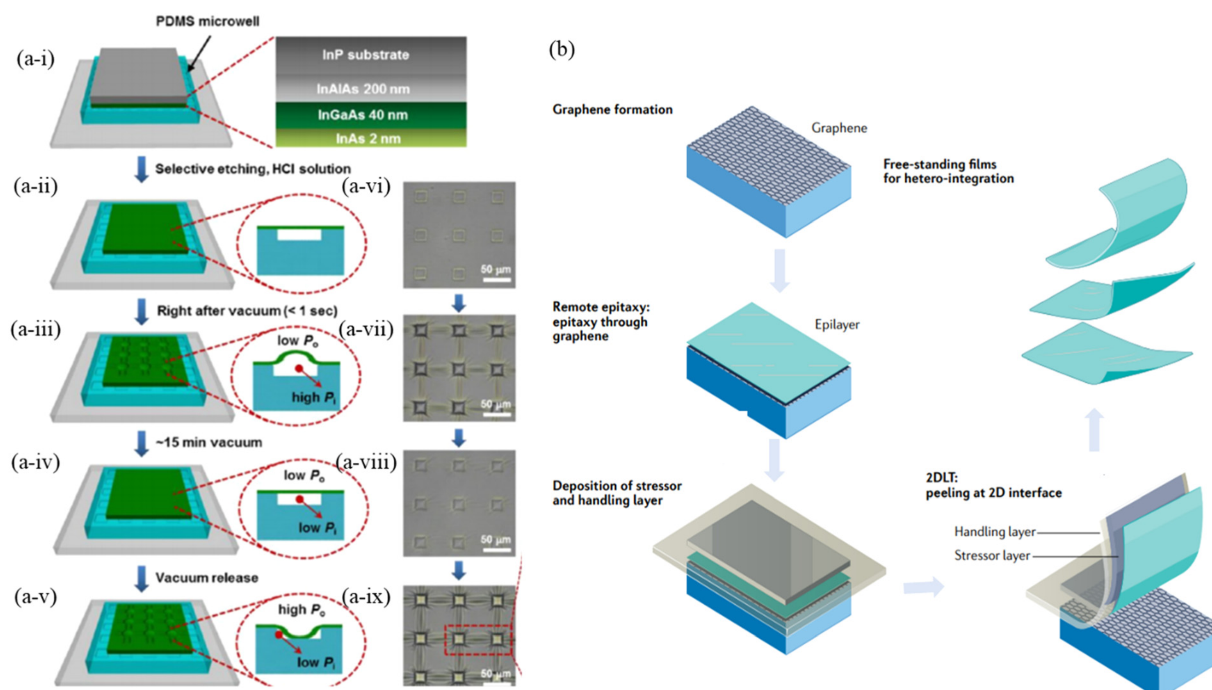

Fig. 6 (a) The vacuum-induced wrinkling of InGaAs NMs on polydimethylsiloxane microwell array: (i–v) Schematic illustration of the fabrication procedure. (vi–ix) A series of optical microscope (OM) images of InGaAs NMs during the vacuum-induced wrinkling process: (vi) before the vacuum process, (vii) right after the vacuum process, (viii) ~15 min after the vacuum process, and (ix) right after the vacuum release.[77] (b) Remote epitaxy and layer transfer process.[78] Reproduced with permission from ref. 77 and 78. Copyright 2014, 2022, American Chemical Society, Springer Nature.

This journal is © The Royal Society of Chemistry 2023

Open Access Article. Published on 20 January 2023. Downloaded on 9/14/2024 7:34:49 AM. This article is licensed under a Creative Commons Attribution-NonCommercial 3.0 Unported Licence.

and fast response time.[76] Despite the competitive advantages of InGaAs, narrow detection range and large dark current restrict its application in optical communication. Therefore, flexible InGaAs NMs provide a means of extending their detection range by band-gap modulation *via* strain engineering. However, little research on InGaAs NMs has been carried out mainly due to the difficulties in releasing high-quality InGaAs NMs.

Similar to the fabrication of GeSn NMs, InGaAs NMs can be released by removing the sacrificial InAlAs layers using hydrochloric acid (HCl). As shown in Fig. 6, wrinkled InGaAs NMs were fabricated by selective wet etching followed by vacuum-induced stretching of locally constrained InGaAs NMs. This technique introduces biaxial strain and therefore provides an approach to modulate carrier mobility and band structure of InGaAs NMs. However, it has the limitation in the choice of the sacrificial layer. In general, InGaAs layer was grown on AlAs/InP substrate using AlAs as a sacrificial layer. Although AlAs could offer high etching selectivity over both the InP substrate and the functional InGaAs layer in HF solution, the lattice mismatch (3.6%) with InP makes it difficult to form high quality InGaAs layers.

Another emerging approach called remote epitaxy has been proposed to overcome the limitation and achieve high-quality single crystalline NMs. GaAs was epitaxy grown on graphene coated bulk GaAs substrate.[79,80] The ultrathin graphene layer allows remote interaction between substrates and epilayers, leading to the formation of crystalline epilayers that continues the substrate crystals.[81,82] GaAs NMs were released after removing graphene layer by wet or dry etching.

3.2. Applications of InGaAs nanomembranes

Recently, InGaAs NMs were developed for applications in optoelectronic devices, such as PDs,[83,84] LEDs,[85] and field effect transistors.[86] For example, D. Fan *et al.* demonstrated a thin-film InGaAs p–i–n PD array fabricated on a thin and flexible polyimide Kapton substrate.[87] The array was transformed into a cylindrical shape to achieve a 360° (*i.e.*, 2π) in-plane field of viewing (FOV). High-performance flexible InGaAs PDs integrated with waveguide were demonstrated, exhibiting a low noise equivalent power of 0.02 pW $Hz^{1/2}$ at room temperature and the telecommunication C-band. Moreover, significant improvements include a large linear dynamic range over 70 dB and 3 dB bandwidth of 1.4 GHz, all of which set new records for flexible detectors, as shown in Fig. 7(a).[88] J. Shi *et al.* also reported InGaAs/InAlAs high electron mobility transistors transferred onto a flexible Kapton substrate employing the adhesive bonding technique. The effect of mechanical bending conditions on electrical performance has been also investigated in static and dynamic regimes.[89] Although InGaAs membrane-based optoelectronic devices outperform Group IV membrane-based devices due to its direct bandgap, the CMOS compatibility and cost are still obstacles for the commercialization. To overcome this problem, a monolithic InP/SOI platform has been developed, where both dislocation-free InP submicron wires and large-dimension InP membranes are selectively grown on (001) SOI wafers and intimately placed with the Si device layer. The InGaAs quantum wells or InAs quantum dots could be selectively regrown on top of the NMs.[90]

Another promising application of narrow band-gap NMs is broadband heterojunction diodes through van der Waals (vdW) bonding, which is of great importance in high-capacity optical communication. Conventional approaches to fabricate heterojunctions such as epitaxial growth or wafer bonding have problems of inferior interface quality due to the lattice mismatch and thermal expansion coefficient mismatch. Thus, heterojunction formed by transfer printed NMs on dissimilar layers is a useful approach to avoid such mismatch issues. High-performance broadband InGaAs NM/Si heterojunction PDs that cover the detection range from 450 to 1250 nm have been demonstrated. The devices exhibited a high rectification

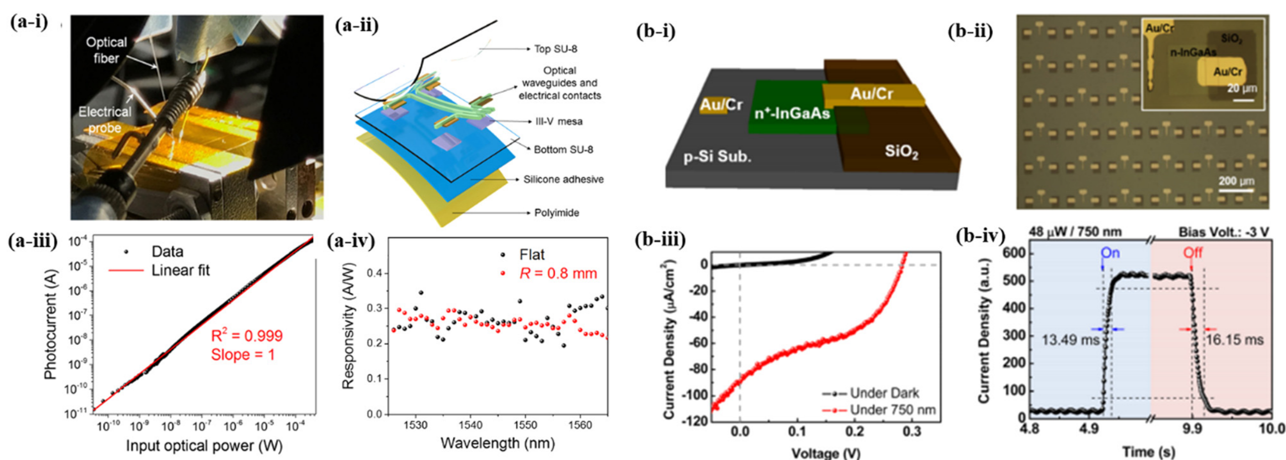

Fig. 7 InGaAs NM optoelectronic device applications: (a-i) Photo during the measurement, (a-ii) schematic structure, (a-iii) double logarithm plot showing the linear dynamic range, (a-iv) spectral response across C-band and bent states of flexible waveguide-integrated InGaAs NM PD.[88] Reproduced with permission from ref. 88. Copyright 2018, Optical Society of America. (b-i) Schematic device structure, (b-ii) Microscopic image of the device, (b-iii) photovoltaic characteristics, and (b-iv) the enlarged current response time at −3 V reverse bias under the 750 nm (48 μW) light illumination of InGaAs NM/Si heterojunction PD.[91] Reproduced with permission from ref. 91. Copyright 2016, American Chemical Society.

Open Access Article. Published on 20 January 2023. Downloaded on 9/14/2024 7:34:49 AM.
This article is licensed under a Creative Commons Attribution-NonCommercial 3.0 Unported Licence.

ratio of 7.73×10^4 at ± 3 V, a low leakage current of 7.44×10^{-5} A cm^{-2} at -3 V, and fast response times of 13–16 ms, owing to the high-quality interface enabled by the transfer printing technique (Fig. 7(b)).[91] This technique has been also applied on GeSn/Si heterostructures formed by transfer printing of Si NMs on GeSn layers with various Sn contents. An increase in the Sn content extended the detection range of GeSn/Si PDs up to 2100 nm.[92] Y. Lee *et al.* have demonstrated an n-InGaAs/BP diode by adopting double-times transfer printing of each NMs onto a SiO_2/Si substrate *via* PDMS stamping.[93] This device offers nonvolatile-memory properties through charge trapping in the native phosphorus oxide, exhibiting unique diode characteristics which are gate-controllable and programmable. These multifunctional properties provide numerous potential applications such as novel advanced logic circuits, controllable electric transformers, and neuromorphic devices. Therefore, the transfer printing technique can be more desirable than other approaches to achieve high-quality heterostructures with dissimilar materials.

4. Black phosphorus

4.1. Fabrication process

BP, one of the most promising NBG 2D materials, is a layered plane of phosphorus monolayer (called phosphorene) with an anisotropic puckered honeycomb structure. The unique material properties of BP include high electron mobility (1000 $cm^2 V^{-1} s^{-1}$), on/off current ratio ($<10^5$),[46,49] anisotropic transport, and tunable direct band-gap (0.3 eV in bulk to 2.0 eV in a single layer).[94,95] Owing to these excellent intrinsic optoelectronic properties, BP has been applied in a wide range of optical and electrical devices such as lasers, PDs, transistors, and logic inverters. Contrary to the NMs, which typically use wafer-scale semiconductor-on-insulator platforms, the fabrication of 2D material NMs relies on exfoliation from bulk crystalline materials using either top-down exfoliation or bottom-up direct growth techniques.

Since the first successful synthesis of bulk BP in 1914 by Bridgman,[96] numerous studies have reported high-quality bulk BP from red or white phosphorus. The high-pressure methods such as the Bridgman and ball milling methods have disadvantages in that they require over 1 GPa pressure with a limitation in the size of synthesized BP (micrometer scale).[97–99] Thus, new approaches have been developed to obtain millimeter-sized bulk BP under low pressure, such as BP synthesis with mercury catalyst,[100] and bismuth-flux,[101,102] or chemical vapor transport.[103,104] The synthesized bulk BP is then used to isolate thin-film BP NMs using isolation techniques, such as mechanical exfoliation, liquid-phase exfoliation (LPE), and electrochemical exfoliation (ECE),[105–107] and herein, the quality of bulk BP is of utmost importance.

The mechanical exfoliation, which is to peel few-layer BP from bulk phosphorus by overcoming vdW attraction between bulk phosphorus flakes, includes micromechanical cleavage with adhesive tape[46,49] and additional subsequent plasma thinning (Fig. 8 (a)).[108,109] For LPE, BP is produced by sonicating dispersed liquid of bulk BP in a solvent followed by centrifugation. Compared to other processes, LPE is suitable for mass production because of its advantages of low-cost, simple, and efficient fabrication. Since the first LPE-synthesized BP was demonstrated by J. R. Brent *et al.* using *N*-methyl-2-pyrrolidone (NMP) solvent,[110] many researchers have shown successful synthesis of BP using LPE by applying multiple solvents: organic solvents such as benzonitrile, DMI, PVP, MF,[111] dimethylformamide (DMF), dimethyl sulfoxide (DMSO),[112] *N*-cyclohexyl-2-pyrrolidone (CHP),[113] IPA,[114,115] and a non-organic solvent such as distilled water.[116] Furthermore, advanced LPE using ionic liquids or solvothermal reactions also have been developed for large-scale, efficient, and facile fabrication.[117,118] For the ECE approach, thin-film BP is isolated from an electrode with bulk BP crystal by applying the voltage between two electrodes, triggering redox reactions between water molecules, electrolytes, and electrodes, and weakening vdW force. (Fig. 8(b)) After the first ECE trial by M. B. Erande *et al.* who demonstrated anodic BP ECE using NA_2SO_4 electrolyte in H_2O,[119] numerous studies have been made with diverse combinations of electrolyte and solvent: anodic ECEs of H_2SO_4 in H_2O,[120] [EMIM][BF_4] in MeCN,[121] [BMIM][PF_6] in MeCN,[122] cathodic ECEs of TBAP in DMF,[123] TAA in DMSO,[124] TBA-HSO_4[125] in PC, and PEAP in PC,[126] and bipolar ECEs.[127,128] Here, while anodic ECE resulted in a dimension of 0.5–5 μm and thickness of 1–10 nm because of the oxidation of BP at the anodic electrode, cathodic ECE has shown a larger dimension over 10 μm and thinner thickness of 0.76–10 nm. Nevertheless, the top-down approaches are considered unsuitable for industrial applications due to the small size of exfoliated BP.

As an alternative approach for wafer-scale mass production, bottom-up methods have been developed which is a direct-growth approach of thin-film BP by chemical vapor deposition (CVD),[129] pulsed laser deposition (PLD),[130,131] gas-phase transformations,[132] and solid–vapor–solid transformation.[133] Although CVD is widely used for 2D material synthesis, the CVD approach exhibited poor performance due to high defect density and poor electrical and optical properties. Although PLD also showed the successful synthesis of BP on a centimeter scale) the method is unsuitable for mass production due to its high cost as well as the low carrier mobility of synthesized BP. Furthermore, there is an additional issue with utilizing few-layer BP at the device level which is its poor stability. High stability can be achieved by applying physical or chemical methods after the preparation of a few-layer BP. The physical method is to cover BP by a passivation layer such as oxides such as Al_2O_3,[134] SiO_2,[135] TiO_2 nanoparticles,[136] or 2D materials (*e.g.* graphene and hBN).[137] The chemical method improves stability through the modification of molecules[138] or metal ions.[139,140] In summary, utilization of BP in optical and electrical devices still has some challenges due to difficulties in synthesizing highly crystalline and large-size BP, as well as improving stability in the air.

4.2. Applications

4.2.1. Flexible NIR PDs. The unique material properties of BP, which are tunable direct band-gap, high carrier mobility, and superior mechanical flexibility, permit their use in flexible optoelectronic device applications. However, little progress has

Open Access Article. Published on 20 January 2023. Downloaded on 9/14/2024 7:34:49 AM.
This article is licensed under a Creative Commons Attribution-NonCommercial 3.0 Unported Licence.

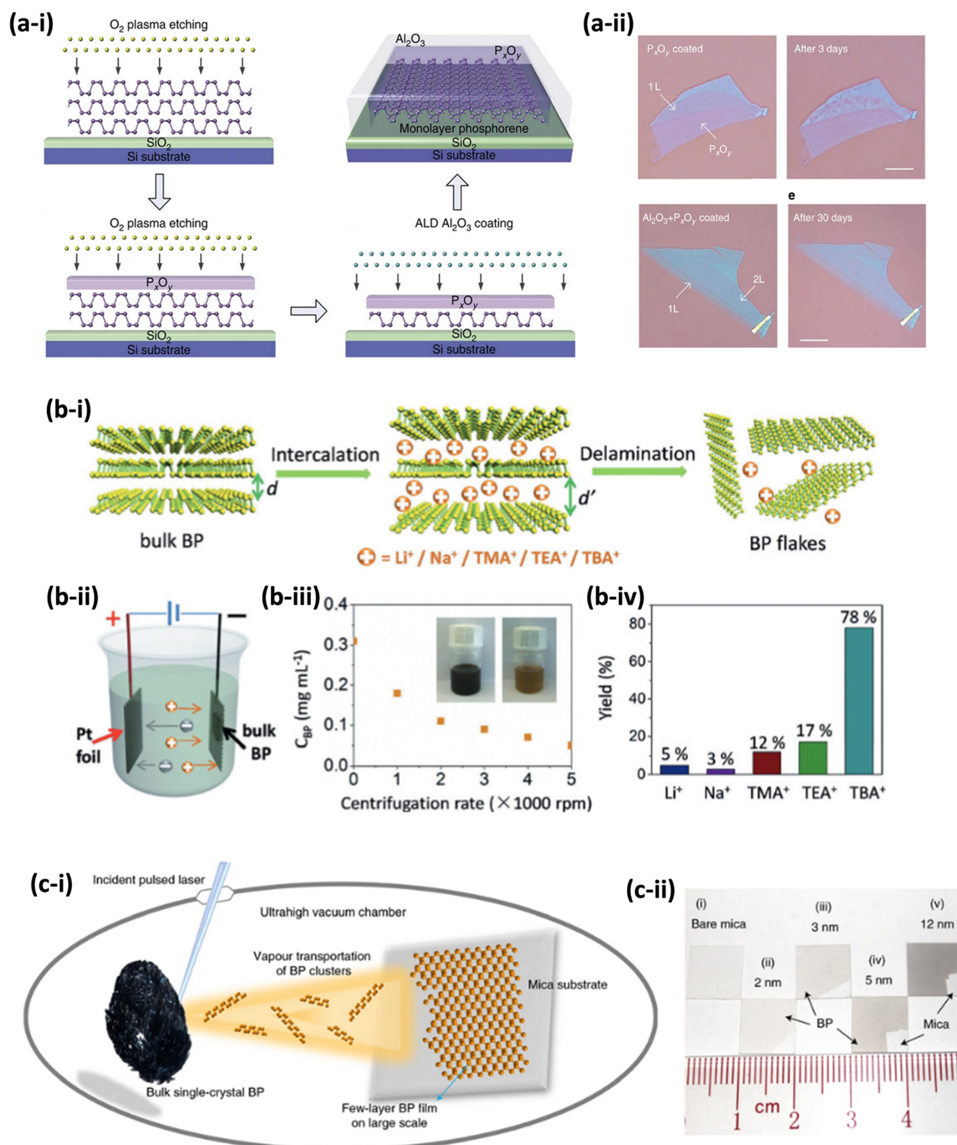

Fig. 8 (a) Mechanically exfoliated black phosphorus (BP) on a SiO_2/Si substrate treated with O_2 plasma etching: (a-i) schematic illustration of the preparation process, and (a-ii) OM images of single-layer BP covered by P_xO_y or P_xO_y/Al_2O_3 capping layer before and after several days.[109] Reproduced with permission from ref. 109. Copyright 2016, Springer Nature. (b): Electrochemically exfoliated BP: (b-i) Schematic delamination procedure, (b-ii) Experimental setup, (b-iii) Concentration of BP as a function of centrifugation rate, and (a-iv) Delamination yield as a function of intercalating cations.[125] Reproduced with permission from ref. 125. Copyright 2016, John Wiley-VCH.

been made for such applications so far, due to its difficult synthesis, high-cost fabrication, and rapid degradation upon exposure to the air.

Using the excellent flexibility of BP reported by Q. Wei *et al.*,[141] the first flexible BP transistor has been demonstrated by W. Zhu *et al.*[142] As described in Fig. 9(a), the device was fabricated by mechanical exfoliation method and exhibited outstanding carrier mobility of 310 $cm^2\ V^{-1}\ s^{-1}$ as well as robust device performance after 5000 cycles of bending with 2% tensile strain. Furthermore, J. Miao *et al.* showed flexible NIR BP PDs which have high responsivity of 53 A W^{-1} under 16.5 W cm^{-2} laser illumination (λ = 830 nm).[143]

Also, a combination of other 2D materials showed an improved photodetection performance. Recently, H. Kim *et al.* demonstrated flexible and strain-tunable IR optoelectronic devices based on BP-MoS_2 heterostructures using mechanical exfoliation.[144] Here, different optoelectronic devices including PD and LED were demonstrated and they showed high detectivity of 5.97×10^9 cm H $w^{1/2}$ W^{-1} at 4.0 μm and 8.45×10^9 cm $Hz^{1/2}$ W^{-1} at 2 μm under compressive and tensile conditions, respectively. Y. Zhou *et al.* also exhibited a superior flexible PD based on bismuth nanosheets–BP quantum dots heterojunctions by sonication-assisted LPE, achieving a photocurrent density of 4.6 μA cm^{-2} at an applied voltage of 0.8 V, and 100 nA cm^{-2} without external voltage.[145] (Fig. 9(b)) For the bending test, the device performance revealed the photocurrent density attenuation of 15% after 2000 times of bending and 8.8% under a bending angle of 60°.

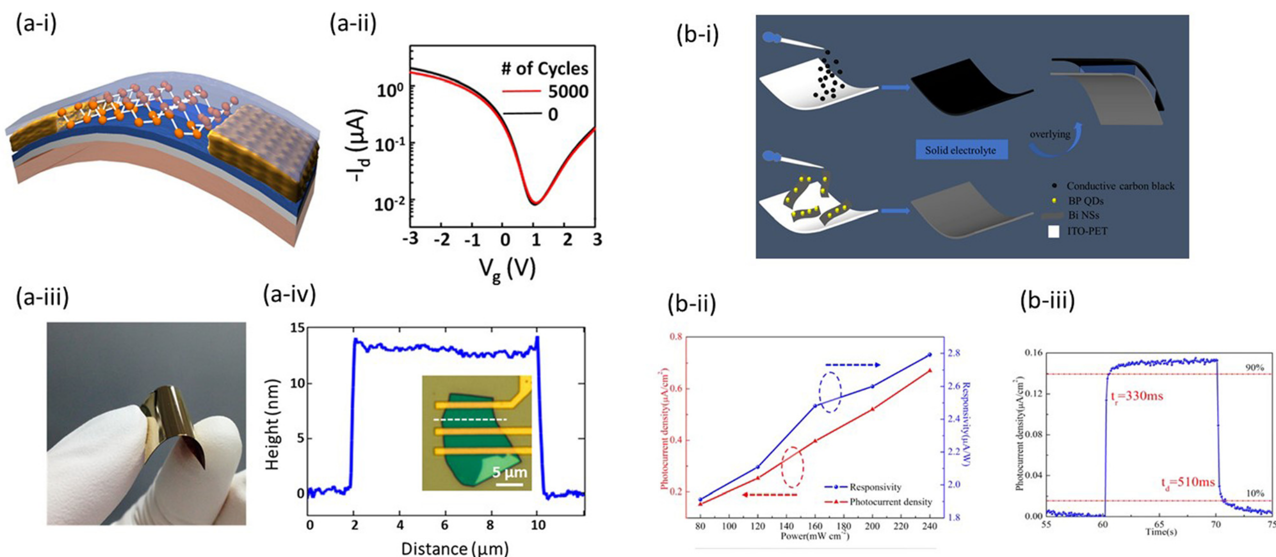

Fig. 9 (a) Flexible BP FETs on a flexible PI substrate: (i) schematic illustration, (ii) I–V characteristics, (iii) Photograph of the device, and (iv) AFM height profile of a few-layer BP flake showing thickness of 13 nm.[142] Reproduced with permission from 142. Copyright 2015, American Chemical Society. (b) Flexible Bi nanosheets-BP quantum dots PDs: (i) Device fabrication process, (ii) photocurrent density and responsivity, and (iii) temporal response.[145] Reproduced with permission from 145. Copyright 2021, American Chemical Society.

4.2.2. Light emitting applications including LEDs and lasers. So far, a few results on BP light emitting devices have been reported because of low luminescence efficiency and challengeable fabrication process. To overcome this obstacle, BP-based MIR lasers which use coupling BP with optical microcavities have been reported. Y. Huang *et al.* applied distributed Bragg reflector (DBR) consisting of stack layers of SiO_2/Si_3N_4 for BP MIR lasers, resulting in an optically pumped lasing at an ~3765 nm MIR range.[146] Furthermore, Y. Zhang *et al.*, reported MIR lasers based on BP coupled with a SiO/Si DBR cavity, and here, stimulated emission at 3611 nm was achieved as well as tuning of lasing wavelength from 3.4 μm to 4.0 μm by controlled BP thickness.[146]

There has been a recent progress in MIR LEDs using BP-based heterostructures. X. Zong *et al.*, demonstrated BP-TMDC heterostructure using either WSe_2 or MoS_2.[147] The BP-based vdWH LED integrated with WSe_2 or MoS_2 showed an ~200% enhancement of the PL intensities in the MIR region due to efficient energy transfer between BP and WSe_2, and MIR lasing at room temperature, respectively. J. Wang *et al.* developed the BP/MoS_2 MIR LEDs emitting at 3.68 μm at room temperature. It showed enhanced outcoupling efficiency *via* the use of low-index or metallic substrate, as well as further improved quantum efficiency *via* heterostructure.[148] Recently, H. Kim *et al.* demonstrated flexible BP MIR LEDs with strain-tunable band-gap characteristics, and observed PL peak shift from 5.5 to 3.2 μm under compressive and tensile strain, respectively.[144]

In this review, we focus on BP's applications in flexible or optoelectronic devices. Although it is not covered in depth, there have been a large number of publications on BP-based electronic devices including transistors, being considered as the primary application area.[149]

5. Graphene

5.1. Fabrication process

Graphene, which is the first discovered 2D material, is a solitary single layer of carbon atoms bonded in a hexagonal honeycomb lattice. The unique material properties of graphene include high carrier mobility (200 000 $cm^2\ V^{-1}\ s^{-1}$),[150] thermal conductivity (5000 $W\ m^{-1}\ K^{-1}$),[151] transparency (97.6%, white light),[152] Young's modulus (1.0 TPa),[153] zero band-gap (0 eV),[40] and novel intrinsic physical properties such as high mechanical, electronic, and thermal transport. Due to its superior properties, a wide range of applications have been discovered in semiconductor devices such as transistors, sensors, supercapacitors, batteries, PDs, solar cells, LEDs, and biomedicines. Furthermore, as a pioneering 2D material, the graphene has been produced by various techniques, which can be divided into two categories; top-down and bottom-up.[154,155] Top-down methods where graphene is isolated from graphite include mechanical exfoliation, LPE, ECE, reduction of graphene oxide (GO), and laser ablation. For the bottom-up approaches, graphene can be directly synthesized on a substrate by CVD, epitaxial growth, arc discharge, and self-assembly.

Mechanical exfoliation is one of the earliest types of graphene synthesis methods, consisting of repeated attach-and-peel-off steps using a sticky tape, also well known as the Scotch tape method discovered by K. S. Novoselov *et al.*[40] (Fig. 10(a)) Not only it is a cost-effective and easy method, but also the material properties of synthesized graphene are remarkable including high carrier mobility and ambipolar field effect.[156] However, the size of mechanically exfoliated graphene is small and inapplicable for mass production, arousing a need for a large-area synthesis method that is economical and applicable for industry.

Open Access Article. Published on 20 January 2023. Downloaded on 9/14/2024 7:34:49 AM. This article is licensed under a Creative Commons Attribution-NonCommercial 3.0 Unported Licence.

Open Access Article. Published on 20 January 2023. Downloaded on 9/14/2024 7:34:49 AM. This article is licensed under a Creative Commons Attribution-NonCommercial 3.0 Unported Licence.

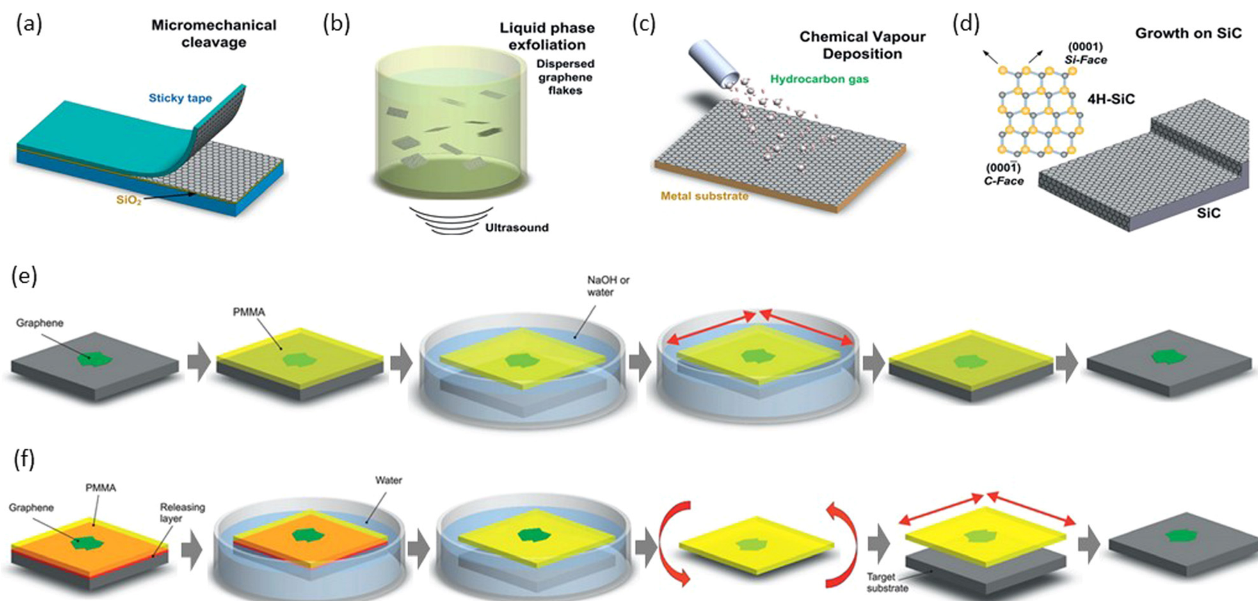

Fig. 10 Graphene synthesis and transfer methods: (a) mechanical exfoliation, (b) liquid phase exfoliation, (c) chemical vapor deposition, (d) growth on SiC, (e) wet transfer and (f) dry transfer method.[155] Reproduced with permission from ref. 155. Copyright 2012, Elsevier Ltd.

Chemical exfoliation includes LPE, reduced GO (rGO), and ECE. LPE which originated in the 1860s[157–159] is a method that isolates graphene from graphite in aqueous solutions by sonication,[160] high-shear mixing, or jet cavitation. So far, sonication-assisted LPE has been vigorously studied under various solvent and sonication conditions[161] (Fig. 10(b)). However, due to the low yields and high energy consumption of sonication-assisted LPE, the emerging LPE methods using high-shear mixing and jet cavitation are preferred over sonication, to be more applicable for production of large-size graphene. Here, high-shear stress can be generated by different methods such as ball milling,[162] tube rotation,[163] and rotor/stator.[164] The jet cavitation method is a green process that can produce graphene in a short time by forcing fluids under pressure to flow through a narrow microchannel, also called the microfluidization method.[161] Another chemical exfoliation approach is to chemically reduce GO, forming rGO by strong acids salts such as $KMnO_4$, $NaNO_3$, and H_2SO_4. This method is also widely used and is well known as Hummers' method.[165] In addition, there have been tremendous studies that showed the successful synthesis of graphene by the ECE approach with additional sonication.[166,167] From the series of studies on ECE, it was found that the sonication-assisted ECE approach can improve the graphene quality and minimize defects under high temperature and ultrasonic waves, becoming the commonly used approach in the science and industrial fields.[34] Laser ablation is an emerging top-down method, having strong advantages in that the process is environmentally friendly, stable, patternable, and applicable on flexible substrates without the usage of harmful reactants. Since the first demonstration of graphene synthesis by laser ablation on polymer films reported by J. Lin *et al.*,[168] laser-ablation synthesis methods using various sources such as wood,[169] cork,[170] and paper,[171] and a wide range of lasers such as UV[172] or Vis radiation,[173] have been reported.

CVD is an ideal method capable of industrial production of high-quality and large-area graphene. The first CVD-grown graphene was reported by Q. Yu *et al.*, exhibiting graphene synthesis on Ni substrate using CH_4, H_2, and Ar gases at 1000 °C.[174] So far, various metallic elements including Ni,[175] Cu,[176] Pd,[177] Pt,[178] and Ir[179] were utilized as a substrate for CVD-grown graphene for a metal catalytic effect (Fig. 10 (c)). CVD-grown graphene has led to superior material properties such as large size single-crystalline graphene and outstanding charge carrier mobility of 350 000 $cm^2\ V^{-1}\ s^{-1}$ at room temperature. However, the limitations of CVD lie in its high cost and challenging transfer onto other substances. Another bottom-up method is the epitaxial growth method through the graphitization of silicon carbide (SiC)[180,181] or hexagonal boron nitride (hBN),[182] which is capable of graphene production with high crystalline quality and charge carrier mobility of $\sim$27 000 $cm^2\ V^{-1}\ s^{-1}$ (Fig. 10(d)). However, the disadvantages of the epitaxial growth method lie in its high-cost SiC substrate and limited size of the synthesized graphene.

After the production process, graphene is transferred through a wet or dry process (Fig. 10(e and f)). As shown in Fig. 10(e), a typical wet transfer is conducted by the following process steps; deposition of a polymethyl methacrylate (PMMA) film on graphene by spin coating; detachment of the PMMA film by wet chemicals; attachment of graphene/PMMA film to a target substrate; drying; dissolution of PMMA by acetone to release graphene on the substrate. On the other hand, graphene can be transferred through dry transfer, as depicted in Fig. 10(f); exfoliation of graphene on water-dissoluble polymer covered by PMMA; floating the sample in water; dissolution of the water-soluble layer; flipping over the graphene/polymer

Open Access Article. Published on 20 January 2023. Downloaded on 9/14/2024 7:34:49 AM. This article is licensed under a Creative Commons Attribution-NonCommercial 3.0 Unported Licence.

film; placement of graphene on a substrate and pressing; dissolution of PMMA.

In summary, there have been numerous studies on graphene synthesis, transfer, and device applications. Additionally, as the material properties of graphene largely rely on the preparation method, the fabrication process should be chosen deliberately to achieve high performance device applications.

5.2. Applications

5.2.1. Flexible NIR PDs. Graphene-based flexible optoelectronics have attracted great attention for wearable devices as graphene is exceedingly thin, strong, light, flexible, and conductive. However, the performance of graphene-based PDs is limited due to low light absorption (~2.3%), fast carrier recombination, and the absence of a bandgap. Therefore, some strategies to overcome these drawbacks have been proposed such as integrating graphene with plasmonic resonators[183,184] or other semiconductor materials such as perovskite,[185] ZnO nanorods,[186] $Cu_{3-x}P$ nanocrystals,[187] NMe_2-GQDs,[188] and Cu_2O quantum dots.[189]

As shown in Fig. 11(a), V. Q. Dang *et al.* reported a flexible graphene/perovskite hybrid PD, achieving excellent device performance of 115 A W^{-1} responsivity at 515 nm as well as 3 × 10^{12} Jones detectivity under 515 nm wavelength light.[185] In this work, $CH_3NH_3PbI_3$ perovskite with a band-gap of 1.5 eV was used as an antenna material, while graphene was a transport layer. The PD also showed a high stable photocurrent under tensile strain (0.5%), which endured 3000 bending cycles. In addition, a graphene/ZnO nanorod hybrid PD was demonstrated and exhibited 2.5 × 10^6 A W^{-1} responsivity and 8.3 × 10^6 photoconductive gain under 5 V gate modulation by inducing the alignment of quasi E_F of ZnO and E_C of graphene. This gate modulation also decreased the energy barrier as well as increased electron transfer from ZnO to graphene simultaneously, showing highly stable device performance with unchanged responsivity under 0.5% tensile strain and 1000 cycles of bending.[186] Nitrogen-functionalized graphene quantum dot (NMe_2-GQD), which has a band-gap of 3.3 eV, was also used to permit graphene to generate photo-induced current under UV light (~255 nm). Using this 2D/0D hybrid structure consisting of graphene/NMe_2-GQD, a flexible UV PD demonstrated an outstanding responsivity of 1.5 × 10^4 A W^{-1} and detectivity of 5.5 × 10^{11} Jones at 255 nm.[188] Recently, flexible PDs based on graphene/CuO_2 quantum dot hybrid structure have been developed by Q. Liu *et al.*, exhibiting excellent responsivity of 1.2 × 10^{10} A W^{-1} and detectivity of 1.4 × 10^{12} Jones at 450 nm as shown in Fig. 11(b).[189] In addition to these results, flexible PDs with graphene electrodes have been reported.[190–192]

5.2.2. Light emitting applications (LED, laser) and other applications. So far, graphene-based ultrashort-pulse lasers have been exploited tremendously owing to their nonlinear absorption property by different types of lasers, including fiber-based,[35,193] solid-state,[194,195] and waveguide lasers.[196] B. Fu *et al.* showed ultrafast broadband graphene fiber lasers covering 1, 1.5, and 2 μm wavelengths. The laser was fabricated by sandwiching three graphene films between two fiber ferrule connectors using CVD growth methods, achieving maximum output energy up to 16.2 nJ at 1.908 μm.[193] A passively mode-locked femtosecond laser with graphene saturable absorber mirror was demonstrated by J. Ma *et al.*, obtaining an average output power of 60.2 mW at 2018 nm.[195] The graphene-based saturable absorber mirror is shown with the light intensity spectrum of the graphene mode-locked laser in the spectral region of 2 μm. Additionally, R. Mary *et al.* demonstrated a monolithic waveguide laser with a graphene-based saturable absorber mirror, which is an output coupler mirror coated by a graphene film.[196] The device performance such as GHz picosecond pulses at ~1.039 μm, with a 1.5 GHz repetition rate,

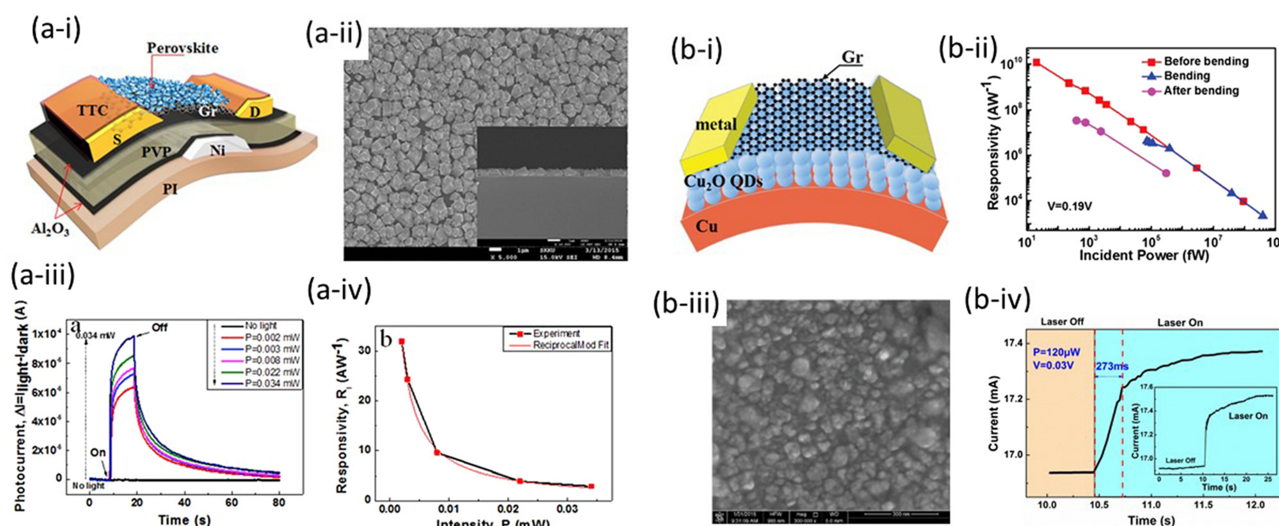

Fig. 11 (a) Graphene/perovskite flexible PDs: (a-i) device schematic, (a-ii) a top-view SEM image, (a-iii) time-dependent photocurrent, and (a-iv) responsivity under different intensities at a 515 nm wavelength and 1 V source-drain voltage.[185] Reproduced with permission from ref. 185. Copyright 2016, Elsevier Ltd. (b) Graphene/Cu_2O quantum dots: (b-i) photodetector structure, (b-ii) responsivity *vs.* incident power under a 450 nm laser, (b-iii) a plan-view SEM image and (b-iv) temporal response.[189] Reproduced with permission from ref. 189. Copyright 2019, Wiley-VCH.

Table 3 Figures of merit of state-of-art flexible photodetectors based on different single-crystalline NBG NMs

Materials	Bias voltage (V)	Dark current	Dark current density	Wavelength (nm)	3-dB (Hz)	Rise time (s)	Responsivity (A/W)	Ref.
Flexible Ge	1	—	9.6 mA cm^{-2}	1550	—	2.2×10^{-3}	0.05	15
Flexible GeSn	2	8.1 μA	0.09 A cm^{-2}	2000	—	—	1.03×10^{-3}	19
Flexible GeSn	2	—	28 mA cm^{-2}	1550	—	—	0.148	65
Flexible InGaAs	5	170 pA	—	1550	1.4×10^{9}	—	0.35	88
Flexible BP	0.3	−20 to −30 μA	—	830	—	—	53	143
Flexible BP	0.1	—	—	1650	10^{3}	18.6×10^{-6}	0.5–2.5	144
Flexible Bi NSs-BP QD	0	—	0.05 uA cm^{-2}	Vis light (Xe lamp)	—	330×10^{-3}	2.8×10^{-6}	145
Flexible graphene/perovskite	1	4.1 mA	—	515	—	3.2	115	185
Flexible graphene/ZnO nanorod	1	3.2 mA	—	365	—	—	2.5×10^{6}	186
Flexible graphene/$Cu_{3-x}P$ NC	1	20 uA	—	405	—	0.42	1.59×10^{5}	187
Flexible graphene/NMe_2-GQD	0.1	1.3 mA	—	255	—	3.7	1.5×10^{4}	188
Flexible graphene/CuO_2 QD	0.19	0.1 A	—	450	—	—	1.2×10^{10}	189

and 202 mW average output power was obtained owing to the combination of the graphene-based mirror and high-quality waveguides in the laser glass.

Like BP, graphene also has been applied in a wide range of electronic devices such as transistors and supercapacitors owing to its high specific capacitance, power density, stability, and fast charge–discharge rate compared to conventional energy storage devices (*e.g.* batteries and capacitors).[36,197] However, we do not provide a review of the widely researched applications of Graphene in electronic devices in detail because our review focuses on flexible optoelectronic devices.

6. Conclusions

In summary, we have presented recent progress in NBG semiconductor NMs from their material preparation to applications in flexible optoelectronic devices, which is provided in Table 3. For the fabrication process, different approaches can be used depending on the materials; Ge, GeSn, and InGaAs NMs. They mainly use a semiconductor-on-insulator platform; meanwhile, 2D materials are typically based on exfoliation procedures. The material characteristics of NBG semiconductors are summarized in this review. We also cover the recent progressive results in their device applications such as flexible optical sensors, van der Waals heterojunction diodes, light emitting diodes, logical inverters, solar cells, *etc.* This broad range of device applications is possible due to their outstanding mechanical and optoelectronic properties, including superb flexibility, high carrier mobility, thin thickness, and easiness to apply strain. Furthermore, advanced techniques, which overcome the drawbacks of the NBG NMs, are reviewed such as strain engineering in GeSn and band-gap tuning of 2D materials by controlling layer thickness or doping. The development of high-performance flexible PDs using 2D materials has been limited because of their challengeable synthesis and fabrication methods, high surface defect density, and poor stability in air and water. For BP, the fabrication process and stability are the main challenges in flexible optoelectronic device applications. To overcome these challenges, the methods to synthesize large-area BP with large grain sizes and low defects should be studied. Also, passivation strategies to reduce surface defects should be investigated and the main causes of the device degradation under the air should be researched. About graphene, which has been studied much longer than BP in terms of its fabrication and applications, zero-bandgap has been one of the main challenges in fabricating heterojunction optoelectronic devices using graphene as a junction. Thus, in-depth studies on the strategies to control the graphene bandgap are required. Further improvement in its synthesis for large-area, low-defect, and highly stable materials and devices are still needed. In conclusion, the NBG NMs will bring exceptional advances in wearable devices or biomedical applications because of their unique material and device characteristics, which cannot be realized by bulk semiconductors.

Conflicts of interest

There are no conflicts to declare.

Acknowledgements

This work was supported by the A*STAR, Singapore, Advanced Manufacturing and Engineering (AME) Young Individual Research Grant (YIRG) and IRG under the Project A2084c0066 and M21K2c0107, respectively, and the Ministry of Education, Singapore, under the Grant ACRF Tier 2 grant (T2EP50120-0001). The authors acknowledge the support of the Nanyang NanoFabrication Centre (N2FC).

References

1 J. Tsao, S. Chowdhury, M. Hollis, D. Jena, N. Johnson, K. Jones, R. Kaplar, S. Rajan, C. Van de Walle and E. Bellotti, *Adv. Electron. Mater.*, 2018, **4**, 1600501.
2 S. An, Y. Liao, S. Shin and M. Kim, *Adv. Mater. Technol.*, 2021, 2100912.
3 S. Su, B. Cheng, C. Xue, W. Wang, Q. Cao, H. Xue, W. Hu, G. Zhang, Y. Zuo and Q. Wang, *Opt. Express*, 2011, **19**, 6400–6405.
4 M. Piccardo, N. A. Rubin, L. Meadowcroft, P. Chevalier, H. Yuan, J. Kimchi and F. Capasso, *Appl. Phys. Lett.*, 2018, **112**, 041106.

Open Access Article. Published on 20 January 2023. Downloaded on 9/14/2024 7:34:49 AM.
This article is licensed under a Creative Commons Attribution-NonCommercial 3.0 Unported Licence.

Open Access Article. Published on 20 January 2023. Downloaded on 9/14/2024 7:34:49 AM.
This article is licensed under a Creative Commons Attribution-NonCommercial 3.0 Unported Licence.

5 J. Zhang, M. A. Itzler, H. Zbinden and J.-W. Pan, *Light: Sci. Appl.*, 2015, **4**, e286–e286.
6 K. Wang, L. W. Yap, S. Gong, R. Wang, S. J. Wang and W. Cheng, *Adv. Funct. Mater.*, 2021, **31**, 2008347.
7 M. Sang, K. Kang, Y. Zhang, H. Zhang, K. Kim, M. Cho, J. Shin, J. H. Hong, T. Kim and S. K. Lee, *Adv. Mater.*, 2022, **34**, 2105865.
8 D. Yadav and D. R. Nair, *IEEE J. Electron Devices Soc.*, 2020, **8**, 308–315.
9 Y. Yang, X. Wang, C. Wang, Y. Song, M. Zhang, Z. Xue, S. Wang, Z. Zhu, G. Liu and P. Li, *Nano Lett.*, 2020, **20**, 3872–3879.
10 I. Yang, Z. Li, J. Wong-Leung, Y. Zhu, Z. Li, N. Gagrani, L. Li, M. N. Lockrey, H. Nguyen and Y. Lu, *Nano Lett.*, 2019, **19**, 3821–3829.
11 K. Chiba, A. Yoshida, K. Tomioka and J. Motohisa, *ACS Photonics*, 2019, **6**, 260–264.
12 J. Valente, T. Godde, Y. Zhang, D. J. Mowbray and H. Liu, *Nano Lett.*, 2018, **18**, 4206–4213.
13 Y.-C. Tai, P.-L. Yeh, S. An, H.-H. Cheng, M. Kim and G.-E. Chang, *Nanotechnology*, 2020, **31**, 445301.
14 A. Zumeit, A. S. Dahiya, A. Christou, D. Shakthivel and R. Dahiya, *npj Flexible Electron.*, 2021, **5**, 1–10.
15 S. An, S. Wu, K.-H. Lee, C. S. Tan, Y.-C. Tai, G.-E. Chang and M. Kim, *ACS Appl. Electron. Mater.*, 2021, 1780–1786.
16 J. Greil, A. Lugstein, C. Zeiner, G. Strasser and E. Bertagnolli, *Nano Lett.*, 2012, **12**, 6230–6234.
17 J. Kim and M. V. Fischetti, *J. Appl. Phys.*, 2010, **108**, 013710.
18 M. El Kurdi, G. Fishman, S. Sauvage and P. Boucaud, *J. Appl. Phys.*, 2010, **107**, 013710.
19 S. An, S. Wu, C. S. Tan, G.-E. Chang, X. Gong and M. Kim, *J. Mater. Chem. C*, 2020, **8**, 13557–13562.
20 M. Kim, J.-H. Seo, Z. Yu, W. Zhou and Z. Ma, *Appl. Phys. Lett.*, 2016, **109**, 051105.
21 Y. Y. Zhang, S. An, Y. Zheng, J. Lai, J. H. Seo, K. H. Lee and M. Kim, *Appl. Electron. Mater.*, 2022, **8**, 2100652.
22 J.-H. Seo, E. Swinnich, Y.-Y. Zhang and M. Kim, *Mater. Res. Lett.*, 2020, **8**, 123–144.
23 J. Lai, M. N. Hasan, E. Swinnich, Z. Tang, S.-H. Shin, M. Kim, P. Zhang and J.-H. Seo, *J. Mater. Chem. C*, 2020, **8**, 14732–14739.
24 S. Mikael, J.-H. Seo, D.-W. Park, M. Kim, H. Mi, A. Javadi, S. Gong and Z. Ma, *Extreme Mech. Lett.*, 2017, **11**, 77–83.
25 M. Kim, H. Mi, M. Cho, J.-H. Seo, W. Zhou, S. Gong and Z. Ma, *Appl. Phys. Lett.*, 2015, **106**, 212107.
26 H.-C. Yuan, J. Shin, G. Qin, L. Sun, P. Bhattacharya, M. G. Lagally, G. K. Celler and Z. Ma, *Appl. Phys. Lett.*, 2009, **94**, 013102.
27 D. Nam, D. Sukhdeo, S.-L. Cheng, A. Roy, K. Chih-Yao Huang, M. Brongersma, Y. Nishi and K. Saraswat, *Appl. Phys. Lett.*, 2012, **100**, 131112.
28 Z. Xia, H. Song, M. Kim, M. Zhou, T. H. Chang, D. Liu, K. Xiong, Z. Yu, Z. Ma and Q. Gan, Photodetecting MOSFET based on ultrathin single-crystal germanium nanomembrane, 2016 *Conference on Lasers and Electro-Optics (CLEO)*, San Jose, CA, USA, 2016, pp. 1–2.
29 M. Kim, J. Park, W. Zhou and Z. Ma, *Inorganic Flexible Optoelectronics*, 2019, pp. 79–116, DOI: 10.1002/9783527813001.ch3.
30 Z. Xia, H. Song, M. Kim, M. Zhou, T.-H. Chang, D. Liu, X. Yin, K. Xiong, H. Mi, X. Wang, F. Xia, Z. Yu, Z. Ma and Q. Gan, *Sci. Adv.*, 2017, **3**, e1602783.
31 M. Cho, J.-H. Seo, M. Kim, J. Lee, D. Liu, W. Zhou, Z. Yu and Z. Ma, *J. Vac. Sci. Technol., B: Nanotechnol. Microelectron.: Mater., Process., Meas., Phenom.*, 2016, **34**, 040604.
32 A. Gassenq, I. Duchemin, Y.-M. Niquet, A. Glière, N. Pauc, A. Chelnokov, V. Reboud and V. Calvo, *IEEE Photonics J.*, 2021, **14**, 1–4.
33 A. Gassenq, K. Guilloy, G. Osvaldo Dias, N. Pauc, D. Rouchon, J.-M. Hartmann, J. Widiez, S. Tardif, F. Rieutord and J. Escalante, *Appl. Phys. Lett.*, 2015, **107**, 191904.
34 K. A. Madurani, S. Suprapto, N. I. Machrita, S. L. Bahar, W. Illiya and F. Kurniawan, *ECS J. Solid State Sci. Technol.*, 2020, **9**, 093013.
35 X. Peng and Y. Yan, *J. Eur. Opt. Soc.*, 2021, **17**, 16.
36 A. Velasco, Y. K. Ryu, A. Boscá, A. Ladrón-de-Guevara, E. Hunt, J. Zuo, J. Pedrós, F. Calle and J. Martinez, *Sustainable Energy Fuels*, 2021, **5**, 1235–1254.
37 X. Chen, J. S. Ponraj, D. Fan and H. Zhang, *Nanoscale*, 2020, **12**, 3513–3534.
38 Y.-Y. Li, B. Gao, Y. Han, B.-K. Chen and J.-Y. Huo, *Front. Phys.*, 2021, **16**, 43301.
39 V. Tran, R. Soklaski, Y. Liang and L. Yang, *Phys. Rev. B: Condens. Matter Mater. Phys.*, 2014, **89**, 235319.
40 K. S. Novoselov, A. K. Geim, S. V. Morozov, D. Jiang, Y. Zhang, S. V. Dubonos, I. V. Grigorieva and A. A. Firsov, *Science*, 2004, **306**, 666–669.
41 M. Poljak, V. Jovanovic, D. Grgec and T. Suligoj, *IEEE Trans. Electron Devices*, 2012, **59**, 1636–1643.
42 P. Kumar, B. S. Bhadoria, S. Kumar, S. Bhowmick, Y. S. Chauhan and A. Agarwal, *Phys. Rev. B*, 2016, **93**, 195428.
43 E. J. G. Santos and E. Kaxiras, *Nano Lett.*, 2013, **13**, 898–902.
44 D. Zhang, X. Hu, D. Liu, X. Lin, W. Wang, Z. Ding, Z. Wang, B. Cheng and C. Xue, 2018.
45 Y. Chuang, C.-Y. Liu, G.-L. Luo and J.-Y. Li, *IEEE Electron Device Lett.*, 2020, **42**, 10–13.
46 L. Li, Y. Yu, G. J. Ye, Q. Ge, X. Ou, H. Wu, D. Feng, X. H. Chen and Y. Zhang, *Nat. Nanotechnol.*, 2014, **9**, 372–377.
47 V. E. Dorgan, M.-H. Bae and E. Pop, *Appl. Phys. Lett.*, 2010, **97**, 082112.
48 K. Moto, N. Saitoh, N. Yoshizawa, T. Suemasu and K. Toko, *Appl. Phys. Lett.*, 2019, **114**, 112110.
49 H. Liu, A. T. Neal, Z. Zhu, Z. Luo, X. Xu, D. Tománek and P. D. Ye, *ACS Nano*, 2014, **8**, 4033–4041.
50 P. Maycock, *Solid-State Electron.*, 1967, **10**, 161–168.
51 Z. Luo, J. Maassen, Y. Deng, Y. Du, R. P. Garrelts, M. S. Lundstrom, P. D. Ye and X. Xu, *Nat. Commun.*, 2015, **6**, 8572.
52 A. A. Balandin, *Nat. Mater.*, 2011, **10**, 569–581.
53 X. Li, Z. Yu, X. Xiong, T. Li, T. Gao, R. Wang, R. Huang and Y. Wu, *Sci. Adv.*, 2019, **5**, eaau3194.

 This journal is © The Royal Society of Chemistry 2023

Open Access Article. Published on 20 January 2023. Downloaded on 9/14/2024 7:34:49 AM.
This article is licensed under a Creative Commons Attribution-NonCommercial 3.0 Unported Licence.

54 S. Gupta, B. Magyari-Köpe, Y. Nishi and K. C. Saraswat, *J. Appl. Phys.*, 2013, **113**, 073707.
55 S. Mellaerts, V. Afanas' ev, J. W. Seo, M. Houssa and J.-P. Locquet, *ACS Appl. Mater. Interfaces*, 2021, **13**, 30941–30949.
56 W. Dou, *High-Sn-content GeSn Alloy towards Room-temperature Mid Infrared Laser*, University of Arkansas, 2018.
57 M. R. Atalla, S. Assali, A. Attiaoui, C. Lemieux-Leduc, A. Kumar, S. Abdi and O. Moutanabbir, *Adv. Funct. Mater.*, 2020, 2006329.
58 C. S. Fenrich, X. Chen, R. Chen, Y.-C. Huang, H. Chung, M.-Y. Kao, Y. Huo, T. I. Kamins and J. S. Harris, *ACS Photonics*, 2016, **3**, 2231–2236.
59 X. Wu, Z. Tian, H. Cong, Y. Wang, R. Edy, G. Huang, Z. Di, C. Xue and Y. Mei, *Nanotechnology*, 2018, **29**, 42LT02.
60 R. Paiella and M. G. Lagally, *Nanomaterials*, 2018, **8**, 407.
61 A. Gok, X. Wang, S. Scott, A. Bhat, H. Yan, A. Pattammattel, E. Nazaretski, Y. S. Chu, Z. Huang, R. M. Osgood, M. G. Lagally and R. Paiella, *ACS Appl. Nano Mater.*, 2021, **4**, 6160–6169.
62 S. An, Y.-C. Tai, K.-C. Lee, S. Shin, H.-H. Cheng, G.-E. Chang and M. Kim, *Nanotechnology*, 2021, 355704.
63 M. R. M. Atalla, S. Assali, A. Attiaoui, C. Lemieux-Leduc, A. Kumar, S. Abdi and O. Moutanabbir, *Adv. Funct. Mater.*, 2021, **31**, 2006329.
64 F. Yasar, W. Fan and Z. Ma, *IEEE Photonics J.*, 2018, **10** 1–9.
65 S. An, Y. Liao and M. Kim, *ACS Appl. Mater. Interfaces*, 2021, **13**, 61396–61403.
66 R. Chen, S. Gupta, Y.-C. Huang, Y. Huo, C. W. Rudy, E. Sanchez, Y. Kim, T. I. Kamins, K. C. Saraswat and J. S. Harris, *Nano Lett.*, 2014, **14**, 37–43.
67 R. Millar, D. Dumas, K. Gallacher, P. Jahandar, C. MacGregor, M. Myronov and D. Paul, *Opt. Express*, 2017, **25**, 25374–25385.
68 V. Reboud, A. Gassenq, N. Pauc, J. Aubin, L. Milord, Q. Thai, M. Bertrand, K. Guilloy, D. Rouchon and J. Rothman, *Appl. Phys. Lett.*, 2017, **111**, 092101.
69 Q. M. Thai, N. Pauc, J. Aubin, M. Bertrand, J. Chrétien, V. Delaye, A. Chelnokov, J.-M. Hartmann, V. Reboud and V. Calvo, *Opt. Express*, 2018, **26**, 32500–32508.
70 Q. Thai, N. Pauc, J. Aubin, M. Bertrand, J. Chrétien, A. Chelnokov, J. Hartmann, V. Reboud and V. Calvo, *Appl. Phys. Lett.*, 2018, **113**, 051104.
71 J. Yin, X. Cui, X. Wang, P. Sookchoo, M. G. Lagally and R. Paiella, *Appl. Phys. Lett.*, 2016, **108**, 241107.
72 A. Elbaz, D. Buca, N. von den Driesch, K. Pantzas, G. Patriarche, N. Zerounian, E. Herth, X. Checoury, S. Sauvage and I. Sagnes, *Nat. Photonics*, 2020, **14**, 375–382.
73 A. Elbaz, R. Arefin, E. Sakat, B. Wang, E. Herth, G. Patriarche, A. Foti, R. Ossikovski, S. Sauvage and X. Checoury, *ACS Photonics*, 2020, **7**, 2713–2722.
74 W. Li, P. Anantha, S. Bao, K. H. Lee, X. Guo, T. Hu, L. Zhang, H. Wang, R. Soref and C. S. Tan, *Appl. Phys. Lett.*, 2016, **109**, 241101.
75 S. Kim, J.-H. Han, J.-P. Shim, H.-j Kim and W. J. Choi, *Opt. Mater. Express*, 2018, **8**, 440–451.
76 J. Ma, Z. Zhang, G. Miao and Y. Zhao, *Jpn. J. Appl. Phys.*, 2015, **54**, 104301.
77 D.-S. Um, S. Lim, Y. Lee, H. Lee, H.-J. Kim, W.-C. Yen, Y.-L. Chueh and H. Ko, *ACS Nano*, 2014, **8**, 3080–3087.
78 H. Kim, C. S. Chang, S. Lee, J. Jiang, J. Jeong, M. Park, Y. Meng, J. Ji, Y. Kwon and X. Sun, *Nat. Rev. Methods Primers*, 2022, **2**, 1–21.
79 H. Kim, K. Lu, Y. Liu, H. S. Kum, K. S. Kim, K. Qiao, S.-H. Bae, S. Lee, Y. J. Ji and K. H. Kim, *ACS Nano*, 2021, **15**, 10587–10596.
80 Y. Kim, S. S. Cruz, K. Lee, B. O. Alawode, C. Choi, Y. Song, J. M. Johnson, C. Heidelberger, W. Kong and S. Choi, *Nature*, 2017, **544**, 340–343.
81 W. Kong, H. Li, K. Qiao, Y. Kim, K. Lee, Y. Nie, D. Lee, T. Osadchy, R. J. Molnar and D. K. Gaskill, *Nat. Mater.*, 2018, **17**, 999–1004.
82 H. Kim, J. C. Kim, Y. Jeong, J. Yu, K. Lu, D. Lee, N. Kim, H. Y. Jeong, J. Kim and S. Kim, *J. Appl. Phys.*, 2021, **130**, 174901.
83 Y. Li, A. Alian, M. Sivan, L. Huang, K. W. Ang, D. Lin, D. Mocuta, N. Collaert and A. V.-Y. Thean, *APL Mater.*, 2019, **7**, 031503.
84 W. Chen, T. Alford, T. Kuech and S. Lau, *Appl. Phys. Lett.*, 2011, **98**, 203509.
85 X. Wang, X. Cui, A. Bhat, D. E. Savage, J. L. Reno, M. G. Lagally and R. Paiella, *Appl. Phys. Lett.*, 2018, **113**, 201105.
86 S. M. Harazim, P. Feng, S. Sanchez, C. Deneke, Y. Mei and O. G. Schmidt, *Nanoscale Res. Lett.*, 2011, **6**, 1–8.
87 D. Fan, K. Lee and S. R. Forrest, *ACS Photonics*, 2016, **3**, 670–676.
88 L. Li, H. Lin, Y. Huang, R.-J. Shiue, A. Yadav, J. Li, J. Michon, D. Englund, K. Richardson and T. Gu, *Optica*, 2018, **5**, 44–51.
89 J. Shi, N. Wichmann, Y. Roelens and S. Bollaert, *Appl. Phys. Lett.*, 2013, **102**, 243503.
90 Z. Yan, Y. Han, L. Lin, Y. Xue, C. Ma, W. K. Ng, K. S. Wong and K. M. Lau, *Light: Sci. Appl.*, 2021, **10**, 1–10.
91 D.-S. Um, Y. Lee, S. Lim, J. Park, W.-C. Yen, Y.-L. Chueh, H.-J. Kim and H. Ko, *ACS Appl. Mater. Interfaces*, 2016, **8**, 26105–26111.
92 S. An, Y. C. Huang, C. Y. Wu, P. R. Huang, G. E. Chang, J. Lai, J. H. Seo and M. Kim, *Adv. Mater. Technol.*, 2022, 2201136.
93 Y. Lee, D.-S. Um, S. Lim, H. Lee, M. P. Kim, T.-Y. Yang, Y.-L. Chueh, H.-J. Kim and H. Ko, *ACS Appl. Mater. Interfaces*, 2019, **11**, 23382–23391.
94 Y. Du, C. Ouyang, S. Shi and M. Lei, *J. Appl. Phys.*, 2010, **107**, 093718.
95 A. N. Rudenko and M. I. Katsnelson, *Phys. Rev. B: Condens. Matter Mater. Phys.*, 2014, **89**, 201408.
96 P. W. Bridgman, *J. Am. Chem. Soc.*, 1914, **36**, 1344–1363.
97 I. Shirotani, *Mol. Cryst. Liq. Cryst.*, 1982, **86**, 203–211.
98 C. Li, Y. Wu, B. Deng, Y. Xie, Q. Guo, S. Yuan, X. Chen, M. Bhuiyan, Z. Wu, K. Watanabe, T. Taniguchi, H. Wang, J. J. Cha, M. Snure, Y. Fei and F. Xia, *Adv. Mater.*, 2018, **30**, 1703748.

View Article Online

Open Access Article. Published on 20 January 2023. Downloaded on 9/14/2024 7:34:49 AM.
This article is licensed under a Creative Commons Attribution-NonCommercial 3.0 Unported Licence.

99 C.-M. Park and H.-J. Sohn, *Adv. Mater.*, 2007, **19**, 2465–2468.
100 H. Krebs, H. Weitz and K. H. Worms, *Z. Anorg. Allg. Chem.*, 1955, **280**, 119–133.
101 A. Brown and S. Rundqvist, *Acta Crystallogr.*, 1965, **19**, 684–685.
102 Y. Maruyama, S. Suzuki, K. Kobayashi and S. Tanuma, *Physica B + C*, 1981, **105**, 99–102.
103 M. Köpf, N. Eckstein, D. Pfister, C. Grotz, I. Krüger, M. Greiwe, T. Hansen, H. Kohlmann and T. Nilges, *J. Cryst. Grow.*, 2014, **405**, 6–10.
104 S. Lange, P. Schmidt and T. Nilges, *Inorg. Chem.*, 2007, **46**, 4028–4035.
105 Y. Yi, X.-F. Yu, W. Zhou, J. Wang and P. K. Chu, *Mater. Sci. Eng., R*, 2017, **120**, 1–33.
106 N. Sultana, A. Degg, S. Upadhyaya, T. Nilges and N. Sen Sarma, *Mater. Adv.*, 2022, **3**, 5557–5574.
107 Y. Zeng and Z. Guo, *iScience*, 2021, **24**, 103116.
108 W. Lu, H. Nan, J. Hong, Y. Chen, C. Zhu, Z. Liang, X. Ma, Z. Ni, C. Jin and Z. Zhang, *Nano Res.*, 2014, **7**, 853–859.
109 J. Pei, X. Gai, J. Yang, X. Wang, Z. Yu, D.-Y. Choi, B. Luther-Davies and Y. Lu, *Nat. Commun.*, 2016, **7**, 10450.
110 J. R. Brent, N. Savjani, E. A. Lewis, S. J. Haigh, D. J. Lewis and P. O'Brien, *Chem. Commun.*, 2014, **50**, 13338–13341.
111 A. H. Woomer, T. W. Farnsworth, J. Hu, R. A. Wells, C. L. Donley and S. C. Warren, *ACS Nano*, 2015, **9**, 8869–8884.
112 P. Yasaei, B. Kumar, T. Foroozan, C. Wang, M. Asadi, D. Tuschel, J. E. Indacochea, R. F. Klie and A. Salehi-Khojin, *Adv. Mater.*, 2015, **27**, 1887–1892.
113 D. Hanlon, C. Backes, E. Doherty, C. S. Cucinotta, N. C. Berner, C. Boland, K. Lee, A. Harvey, P. Lynch, Z. Gholamvand, S. Zhang, K. Wang, G. Moynihan, A. Pokle, Q. M. Ramasse, N. McEvoy, W. J. Blau, J. Wang, G. Abellan, F. Hauke, A. Hirsch, S. Sanvito, D. D. O'Regan, G. S. Duesberg, V. Nicolosi and J. N. Coleman, *Nat. Commun.*, 2015, **6**, 8563.
114 W. Chen, K. Li, Y. Wang, X. Feng, Z. Liao, Q. Su, X. Lin and Z. He, *J. Phys. Chem. Lett.*, 2017, **8**, 591–598.
115 K. Chen, Y. Wang, J. Liu, J. Kang, Y. Ge, W. Huang, Z. Lin, Z. Guo, Y. Zhang and H. Zhang, *Nanoscale*, 2019, **11**, 16852–16859.
116 H. U. Lee, S. Y. Park, S. C. Lee, S. Choi, S. Seo, H. Kim, J. Won, K. Choi, K. S. Kang, H. G. Park, H.-S. Kim, H. R. An, K.-H. Jeong, Y.-C. Lee and J. Lee, *Small*, 2016, **12**, 214–219.
117 W. Zhao, Z. Xue, J. Wang, J. Jiang, X. Zhao and T. Mu, *ACS Appl. Mater. Interfaces*, 2015, **7**, 27608–27612.
118 B. Tian, B. Tian, B. Smith, M. C. Scott, Q. Lei, R. Hua, Y. Tian and Y. Liu, *Proc. Natl. Acad. Sci. U. S. A.*, 2018, **115**, 4345–4350.
119 M. B. Erande, S. R. Suryawanshi, M. A. More and D. J. Late, *Eur. J. Inorg. Chem.*, 2015, 3102–3107.
120 A. Ambrosi, Z. Sofer and M. Pumera, *Angew. Chem., Int. Ed.*, 2017, **56**, 10443–10445.
121 X. Tang, W. Liang, J. Zhao, Z. Li, M. Qiu, T. Fan, C. S. Luo, Y. Zhou, Y. Li, Z. Guo, D. Fan and H. Zhang, *Small*, 2017, **13**, 1702739.
122 Y. Wang, F. Zhang, X. Tang, X. Chen, Y. Chen, W. Huang, Z. Liang, L. Wu, Y. Ge, Y. Song, J. Liu, D. Zhang, J. Li and H. Zhang, *Laser Photonics Rev.*, 2018, **12**, 1800016.
123 Z. Huang, H. Hou, Y. Zhang, C. Wang, X. Qiu and X. Ji, *Adv. Mater.*, 2017, **29**, 1702372.
124 J. Li, C. Chen, S. Liu, J. Lu, W. P. Goh, H. Fang, Z. Qiu, B. Tian, Z. Chen, C. Yao, W. Liu, H. Yan, Y. Yu, D. Wang, Y. Wang, M. Lin, C. Su and J. Lu, *Chem. Mater.*, 2018, **30**, 2742–2749.
125 S. Yang, K. Zhang, A. G. Ricciardulli, P. Zhang, Z. Liao, M. R. Lohe, E. Zschech, P. W. M. Blom, W. Pisula, K. Müllen and X. Feng, *Angew. Chem., Int. Ed.*, 2018, **57**, 4677–4681.
126 L. Zu, X. Gao, H. Lian, C. Li, Q. Liang, Y. Liang, X. Cui, Y. Liu, X. Wang and X. Cui, *J. Alloys Compd.*, 2019, **770**, 26–34.
127 C. C. Mayorga-Martinez, N. Mohamad Latiff, A. Y. S. Eng, Z. Sofer and M. Pumera, *Anal. Chem.*, 2016, **88**, 10074–10079.
128 A. Rabiei Baboukani, I. Khakpour, V. Drozd, A. Allagui and C. Wang, *J. Mater. Chem. A*, 2019, **7**, 25548–25556.
129 J. B. Smith, D. Hagaman and H.-F. Ji, *Nanotechnology*, 2016, **27**, 215602.
130 Z. Yang, J. Hao, S. Yuan, S. Lin, H. M. Yau, J. Dai and S. P. Lau, *Adv. Mater.*, 2015, **27**, 3748–3754.
131 Z. Wu, Y. Lyu, Y. Zhang, R. Ding, B. Zheng, Z. Yang, S. P. Lau, X. H. Chen and J. Hao, *Nat. Mater.*, 2021, **20**, 1203–1209.
132 Y. Xu, J. Yuan, L. Fei, X. Wang, Q. Bao, Y. Wang, K. Zhang and Y. Zhang, *Small*, 2016, **12**, 5000–5007.
133 Y. Zhang, X. Rui, Y. Tang, Y. Liu, J. Wei, S. Chen, W. R. Leow, W. Li, Y. Liu, J. Deng, B. Ma, Q. Yan and X. Chen, *Adv. Energy Mater.*, 2016, **6**, 1502409.
134 J. Na, Y. T. Lee, J. A. Lim, D. K. Hwang, G.-T. Kim, W. K. Choi and Y.-W. Song, *ACS Nano*, 2014, **8**, 11753–11762.
135 B. Wan, B. Yang, Y. Wang, J. Zhang, Z. Zeng, Z. Liu and W. Wang, *Nanotechnology*, 2015, **26**, 435702.
136 H. Uk Lee, S. C. Lee, J. Won, B.-C. Son, S. Choi, Y. Kim, S. Y. Park, H.-S. Kim, Y.-C. Lee and J. Lee, *Sci. Rep.*, 2015, **5**, 8691.
137 R. A. Doganov, E. C. T. O'Farrell, S. P. Koenig, Y. Yeo, A. Ziletti, A. Carvalho, D. K. Campbell, D. F. Coker, K. Watanabe, T. Taniguchi, A. H. C. Neto and B. Özyilmaz, *Nat. Commun.*, 2015, **6**, 6647.
138 C. R. Ryder, J. D. Wood, S. A. Wells, Y. Yang, D. Jariwala, T. J. Marks, G. C. Schatz and M. C. Hersam, *Nat. Chem.*, 2016, **8**, 597–602.
139 W. Gu, X. Pei, Y. Cheng, C. Zhang, J. Zhang, Y. Yan, C. Ding and Y. Xian, *ACS Sens.*, 2017, **2**, 576–582.
140 D. Tofan, Y. Sakazaki, K. L. Walz Mitra, R. Peng, S. Lee, M. Li and A. Velian, *Angew. Chem., Int. Ed.*, 2021, **60**, 8329–8336.
141 Q. Wei and X. Peng, *Appl. Phys. Lett.*, 2014, **104**, 251915.
142 W. Zhu, M. N. Yogeesh, S. Yang, S. H. Aldave, J.-S. Kim, S. Sonde, L. Tao, N. Lu and D. Akinwande, *Nano Lett.*, 2015, **15**, 1883–1890.

This journal is © The Royal Society of Chemistry 2023

Open Access Article. Published on 20 January 2023. Downloaded on 9/14/2024 7:34:49 AM.
This article is licensed under a Creative Commons Attribution-NonCommercial 3.0 Unported Licence.

143 J. Miao, B. Song, Q. Li, L. Cai, S. Zhang, W. Hu, L. Dong and C. Wang, *ACS Nano*, 2017, **11**, 6048–6056.

144 H. Kim, S. Z. Uddin, D.-H. Lien, M. Yeh, N. S. Azar, S. Balendhran, T. Kim, N. Gupta, Y. Rho, C. P. Grigoropoulos, K. B. Crozier and A. Javey, *Nature*, 2021, **596**, 232–237.

145 Y. Zhou, H. Qiao, Z. Huang, Q. Ma, F. Liu, G. Liao, S. Luo, J. Zhong and X. Qi, *ACS Sustainable Chem. Eng.*, 2021, **9**, 14918–14926.

146 Y. Zhang, S. Wang, S. Chen, Q. Zhang, X. Wang, X. Zhu, X. Zhang, X. Xu, T. Yang, M. He, X. Yang, Z. Li, X. Chen, M. Wu, Y. Lu, R. Ma, W. Lu and A. Pan, *Adv. Mater.*, 2020, **32**, 1808319.

147 X. Zong, H. Hu, G. Ouyang, J. Wang, R. Shi, L. Zhang, Q. Zeng, C. Zhu, S. Chen, C. Cheng, B. Wang, H. Zhang, Z. Liu, W. Huang, T. Wang, L. Wang and X. Chen, *Light: Sci. Appl.*, 2020, **9**, 114.

148 J. Wang, A. Rousseau, M. Yang, T. Low, S. Francoeur and S. Kéna-Cohen, *Nano Lett.*, 2020, **20**, 3651–3655.

149 A. Pon, A. Bhattacharyya and R. Rathinam, *J. Electron. Mater.*, 2021, **50**, 6020–6036.

150 X. Du, I. Skachko, A. Barker and E. Y. Andrei, *Nat. Nanotechnol.*, 2008, **3**, 491–495.

151 A. A. Balandin, S. Ghosh, W. Bao, I. Calizo, D. Teweldebrhan, F. Miao and C. N. Lau, *Nano Lett.*, 2008, **8**, 902–907.

152 R. R. Nair, P. Blake, A. N. Grigorenko, K. S. Novoselov, T. J. Booth, T. Stauber, N. M. R. Peres and A. K. Geim, *Science*, 2008, **320**, 1308.

153 C. Lee, X. Wei, J. W. Kysar and J. Hone, *Science*, 2008, **321**, 385–388.

154 K. S. Novoselov, V. I. Fal′ko, L. Colombo, P. R. Gellert, M. G. Schwab and K. Kim, *Nature*, 2012, **490**, 192–200.

155 F. Bonaccorso, A. Lombardo, T. Hasan, Z. Sun, L. Colombo and A. C. Ferrari, *Mater. Today*, 2012, **15**, 564–589.

156 A. H. Castro Neto, F. Guinea, N. M. R. Peres, K. S. Novoselov and A. K. Geim, *Rev. Mod. Phys.*, 2009, **81**, 109–162.

157 B. C. Brodie, *Philos. Trans. R. Soc. London*, 1859, **149**, 249–259.

158 L. Staudenmaier, *Ber. Dtsch. Chem. Ges.*, 1898, **31**, 1481–1487.

159 D. Li, M. B. Müller, S. Gilje, R. B. Kaner and G. G. Wallace, *Nat. Nanotechnol.*, 2008, **3**, 101–105.

160 Y. Hernandez, V. Nicolosi, M. Lotya, F. M. Blighe, Z. Sun, S. De, I. T. McGovern, B. Holland, M. Byrne, Y. K. Gun'Ko, J. J. Boland, P. Niraj, G. Duesberg, S. Krishnamurthy, R. Goodhue, J. Hutchison, V. Scardaci, A. C. Ferrari and J. N. Coleman, *Nat. Nanotechnol.*, 2008, **3**, 563–568.

161 Y. Xu, H. Cao, Y. Xue, B. Li and W. Cai, *Nanomaterials*, 2018, **8**, 942.

162 Y. Hernandez, M. Lotya, D. Rickard, S. D. Bergin and J. N. Coleman, *Langmuir*, 2010, **26**, 3208–3213.

163 X. Chen, J. F. Dobson and C. L. Raston, *Chem. Commun.*, 2012, **48**, 3703–3705.

164 K. R. Paton, E. Varrla, C. Backes, R. J. Smith, U. Khan, A. O'Neill, C. Boland, M. Lotya, O. M. Istrate, P. King, T. Higgins, S. Barwich, P. May, P. Puczkarski, I. Ahmed, M. Moebius, H. Pettersson, E. Long, J. Coelho, S. E. O'Brien, E. K. McGuire, B. M. Sanchez, G. S. Duesberg, N. McEvoy, T. J. Pennycook, C. Downing, A. Crossley, V. Nicolosi and J. N. Coleman, *Nat. Mater.*, 2014, **13**, 624–630.

165 W. S. Hummers and R. E. Offeman, *J. Am. Chem. Soc.*, 1958, **80**, 1339.

166 K. Parvez, R. Li, S. R. Puniredd, Y. Hernandez, F. Hinkel, S. Wang, X. Feng and K. Müllen, *ACS Nano*, 2013, **7**, 3598–3606.

167 A. J. Cooper, N. R. Wilson, I. A. Kinloch and R. A. W. Dryfe, *Carbon*, 2014, **66**, 340–350.

168 J. Lin, Z. Peng, Y. Liu, F. Ruiz-Zepeda, R. Ye, E. L. G. Samuel, M. J. Yacaman, B. I. Yakobson and J. M. Tour, *Nat. Commun.*, 2014, **5**, 5714.

169 R. Ye, D. K. James and J. M. Tour, *Acc. Chem. Res.*, 2018, **51**, 1609–1620.

170 A. F. Carvalho, A. J. S. Fernandes, R. Martins, E. Fortunato and F. M. Costa, *Adv. Mater. Technol.*, 2020, **5**, 2000630.

171 B. Kulyk, B. F. R. Silva, A. F. Carvalho, S. Silvestre, A. J. S. Fernandes, R. Martins, E. Fortunato and F. M. Costa, *ACS Appl. Mater. Interfaces*, 2021, **13**, 10210–10221.

172 A. F. Carvalho, A. J. S. Fernandes, C. Leitão, J. Deuermeier, A. C. Marques, R. Martins, E. Fortunato and F. M. Costa, *Adv. Funct. Mater.*, 2018, **28**, 1805271.

173 Z. Zhang, M. Song, J. Hao, K. Wu, C. Li and C. Hu, *Carbon*, 2018, **127**, 287–296.

174 Q. Yu, J. Lian, S. Siriponglert, H. Li, Y. P. Chen and S.-S. Pei, *Appl. Phys. Lett.*, 2008, **93**, 113103.

175 K. S. Kim, Y. Zhao, H. Jang, S. Y. Lee, J. M. Kim, K. S. Kim, J.-H. Ahn, P. Kim, J.-Y. Choi and B. H. Hong, *Nature*, 2009, **457**, 706–710.

176 X. Li, W. Cai, J. An, S. Kim, J. Nah, D. Yang, R. Piner, A. Velamakanni, I. Jung, E. Tutuc, S. K. Banerjee, L. Colombo and R. S. Ruoff, *Science*, 2009, **324**, 1312–1314.

177 S.-Y. Kwon, C. V. Ciobanu, V. Petrova, V. B. Shenoy, J. Bareño, V. Gambin, I. Petrov and S. Kodambaka, *Nano Lett.*, 2009, **9**, 3985–3990.

178 B. J. Kang, J. H. Mun, C. Y. Hwang and B. J. Cho, *J. Appl. Phys.*, 2009, **106**, 104309.

179 J. Coraux, A. T. N'Diaye, C. Busse and T. Michely, *Nano Lett.*, 2008, **8**, 565–570.

180 C. Berger, Z. Song, X. Li, X. Wu, N. Brown, C. Naud, D. Mayou, T. Li, J. Hass, A. N. Marchenkov, E. H. Conrad, P. N. First and W. A. D. Heer, *Science*, 2006, **312**, 1191–1196.

181 S. Y. Zhou, G. H. Gweon, A. V. Fedorov, P. N. First, W. A. de Heer, D. H. Lee, F. Guinea, A. H. Castro Neto and A. Lanzara, *Nat. Mater.*, 2007, **6**, 770–775.

182 G. Giovannetti, P. A. Khomyakov, G. Brocks, P. J. Kelly and J. van den Brink, *Phys. Rev. B: Condens. Matter Mater. Phys.*, 2007, **76**, 073103.

183 Z. Fang, Z. Liu, Y. Wang, P. M. Ajayan, P. Nordlander and N. J. Halas, *Nano Lett.*, 2012, **12**, 3808–3813.

184 M. Freitag, T. Low, W. Zhu, H. Yan, F. Xia and P. Avouris, *Nat. Commun.*, 2013, **4**, 1951.

185 V. Q. Dang, G.-S. Han, T. Q. Trung, L. T. Duy, Y.-U. Jin, B.-U. Hwang, H.-S. Jung and N.-E. Lee, *Carbon*, 2016, **105**, 353–361.

Open Access Article. Published on 20 January 2023. Downloaded on 9/14/2024 7:34:49 AM. This article is licensed under a Creative Commons Attribution-NonCommercial 3.0 Unported Licence.

186 V. Q. Dang, T. Q. Trung, L. T. Duy, B.-Y. Kim, S. Siddiqui, W. Lee and N.-E. Lee, *ACS Appl. Mater. Interfaces*, 2015, **7**, 11032–11040.

187 T. Sun, Y. Wang, W. Yu, Y. Wang, Z. Dai, Z. Liu, B. N. Shivananju, Y. Zhang, K. Fu, B. Shabbir, W. Ma, S. Li and Q. Bao, *Small*, 2017, **13**, 1701881.

188 H. Tetsuka, *Sci. Rep.*, 2017, **7**, 5544.

189 Q. Liu, H. Tian, J. Li, A. Hu, X. He, M. Sui and X. Guo, *Adv. Opt. Mater.*, 2019, **7**, 1900455.

190 S. Liu, Z. Huang, H. Qiao, R. Hu, Q. Ma, K. Huang, H. Li and X. Qi, *Nanoscale Adv.*, 2020, **2**, 906–912.

191 J. M. Kim, S. Kim and S.-H. Choi, *ACS Sustainable Chem. Eng.*, 2019, **7**, 734–739.

192 P. Han, L. St Marie, Q. X. Wang, N. Quirk, A. El Fatimy, M. Ishigami and P. Barbara, *Nanotechnology*, 2018, **29**, 20LT01.

193 B. Fu, Y. Hua, X. Xiao, H. Zhu, Z. Sun and C. Yang, *IEEE J. Sel. Top. Quantum Electron.*, 2014, **20**, 411–415.

194 A. A. Lagatsky, Z. Sun, T. S. Kulmala, R. S. Sundaram, S. Milana, F. Torrisi, O. L. Antipov, Y. Lee, J. H. Ahn, C. T. A. Brown, W. Sibbett and A. C. Ferrari, *Appl. Phys. Lett.*, 2013, **102**, 013113.

195 J. Ma, G. Q. Xie, P. Lv, W. L. Gao, P. Yuan, L. J. Qian, H. H. Yu, H. J. Zhang, J. Y. Wang and D. Y. Tang, *Opt. Lett.*, 2012, **37**, 2085–2087.

196 R. Mary, G. Brown, S. J. Beecher, F. Torrisi, S. Milana, D. Popa, T. Hasan, Z. Sun, E. Lidorikis, S. Ohara, A. C. Ferrari and A. K. Kar, *Opt. Express*, 2013, **21**, 7943–7950.

197 Q. Ke and J. Wang, *J. Materiomics*, 2016, **2**, 37–54.

This journal is © The Royal Society of Chemistry 2023